PREFACE TO THE EDITION

It is with great pleasure that we present the forthcoming issue of the **International Journal of Pure Science Research Studies (IJPSRS)**, a collection that reflects the expanding frontiers of contemporary scientific inquiry and the enduring pursuit of fundamental knowledge across the natural sciences, mathematics, and computational research. The articles featured in this issue collectively demonstrate the dynamic interplay between theoretical foundations, technological advancement, and global scientific challenges, highlighting the essential role of pure science in shaping future innovation and understanding.

The issue opens with an insightful review on coral reef biodiversity and thermal bleaching responses under climate change, addressing one of the most urgent environmental crises of the modern era. By examining the biological and ecological mechanisms underlying coral bleaching, the study presents a comprehensive synthesis of climate-driven reef degradation and emphasizes the necessity of coordinated conservation and climate mitigation strategies for the preservation of marine ecosystems.

Advancing into the domain of computational and mathematical sciences, the issue includes a rigorous exploration of graph neural networks and their mathematical foundations. The article provides a valuable analytical overview of graph-based deep learning architectures, bridging graph theory, spectral analysis, and artificial intelligence. Its discussion of expressive power, message-passing frameworks, and emerging higher-order extensions reflects the growing significance of graph-based machine learning in scientific and industrial applications.

The remarkable progress of modern astrophysics is represented through a detailed review of gravitational wave astronomy. Tracing the evolution of the field from the first LIGO detection to contemporary multi-messenger astronomy, the paper examines both the technological sophistication of interferometric detectors and the profound astrophysical implications of gravitational-wave observations. The discussion of future observatories and cosmological applications demonstrates the transformative impact of this emerging observational science.

This issue also presents a comparative study of numerical methods for nonlinear partial differential equations, an area central to scientific computing and mathematical modelling. Through analytical and computational comparisons of finite difference, finite element, and spectral methods, the article offers meaningful guidance for researchers engaged in solving complex nonlinear systems encountered across physics, engineering, and applied mathematics.

Completing the volume is a comprehensive review of quantum entanglement and its applications in quantum information science. By connecting foundational quantum theory with cutting-edge developments in quantum communication, computation, and cryptography, the article illustrates how one of the most intriguing concepts in modern physics has evolved into a cornerstone of next-generation technologies.

Taken together, the contributions in this issue reflect the interdisciplinary vitality of pure science research and its continuing capacity to address both foundational questions and contemporary global challenges. The studies presented herein not only deepen scientific understanding but also encourage future investigations that transcend disciplinary boundaries and foster collaborative innovation.

The editorial team of International Journal of Pure Science Research Studies (IJPSRS) extends sincere appreciation to all authors, reviewers, editors, and academic contributors whose dedication and scholarly commitment have made this issue possible. We hope that the research published in this volume will inspire meaningful academic dialogue, stimulate further discovery, and contribute significantly to the advancement of scientific knowledge worldwide.

Dr. Sandhya E
Chief editor

CONTENTS

INTERNATIONAL JOURNAL OF PURE SCIENCE RESEARCH STUDIES (IJPSRS)
(Open Access, Double-Blind Peer Reviewed Journal)
ISSN Online: ISSN Print
EDU SCHOOL ijpsrs.com

Coral Reef Biodiversity and Thermal Bleaching Responses under Climate Change

Nishi Ann

Associate Professor, Department Of Zoology, Providence Women's College (Autonomous) Calicut, Kerala, India

Article Information

Received: 2nd February 2026
Received in revised form: 4th March 2026
Accepted: 6th April 2026
Available online: 14th May 2026

Volume: 2
Issue: 2
DOI: https://doi.org/10.5281/zenodo.20150642

Abstract

Coral reefs occupy less than one percent of the ocean floor but host approximately a quarter of described marine species. Climate-driven sea-surface warming has produced five global mass-bleaching events since 1998, with the 2014–2017 event inflicting unprecedented coral mortality on the Great Barrier Reef and other systems.[1,2] This paper reviews the biology of reef-building corals and their obligate endosymbionts, the thermal physiology of bleaching, the documented global bleaching record, and the prospects for adaptation, assisted evolution, and ecosystem-based conservation. Quantitative region-wise coral-cover declines are summarised. The paper concludes that meaningful long-term reef persistence requires atmospheric-CO_2 stabilisation well below 2°C warming, supplemented by locally targeted reduction of compounding stressors and selective reef-restoration programmes.

Keywords: Coral Reef, Mass Bleaching, Symbiodiniaceae, Thermal Stress, Degree Heating Weeks, Conservation Biology.

1. INTRODUCTION

Coral reefs are among the most biologically diverse and economically valuable ecosystems on Earth. Though occupying less than one per cent of the ocean floor, they harbour approximately 25 per cent of described marine species from crustaceans and molluscs to fishes and reef-associated microbial communities. Reef-building scleractinian corals form calcium-carbonate frameworks that support fisheries feeding hundreds of millions of people, protect coastlines from storm damage and erosion, and generate tourism revenue exceeding US$36 billion annually.[3] Global economic valuations of reef ecosystem services, combining fisheries, tourism, coastal protection, and cultural value, reach US$10 trillion per year at contemporary discount rates, underscoring the scale of human dependence on reef persistence.

Corals derive most of their energy (up to 95 per cent in some species) from photosynthetic dinoflagellate endosymbionts of the family Symbiodiniaceae formerly the single genus Symbiodinium, now reclassified into seven genera reflecting deep evolutionary divergences first identified genetically in the 1990s. The symbiosis is thermally narrow: corals typically bleach when sea-surface temperatures exceed the local long-term summer maximum by approximately 1°C for several weeks. Elevated temperatures trigger expulsion or degradation of symbionts (bleaching) that, if prolonged, leads to coral mortality.[4,5] Recovery from bleaching is possible if thermal stress subsides before mortality, but recurrent bleaching prevents full recovery and progressively shifts reef communities toward weedy, thermally tolerant species with reduced structural complexity.

Since 1980 the frequency and severity of mass-bleaching events has increased in parallel with climate-driven ocean warming. The 1998 El Niño-associated event killed roughly 16 per cent of the world's corals; the

2014–2017 third global event affected more than 75 per cent of tropical reefs and caused catastrophic mortality on the Great Barrier Reef, with back-to-back bleaching in 2016 and 2017 killing approximately half of shallow-water corals in the northern sector.[1,6] A fourth global event was declared by NOAA in 2023, ongoing at the time of writing. Under projected emission trajectories consistent with current policy, the IPCC Special Report on 1.5 °C estimated that 70–90 per cent of coral cover would be lost at 1.5 °C of warming, and over 99 per cent at 2 °C.

This paper reviews the biology of reef-building corals and their obligate endosymbionts, the thermal physiology of bleaching, the documented global bleaching record, and the prospects for adaptation, assisted evolution, and ecosystem-based conservation. Quantitative region-wise coral-cover declines are summarised and placed in the context of complementary stressors including ocean acidification, disease outbreaks, and local anthropogenic pressures.

2. CORAL REEF ECOSYSTEM STRUCTURE

Modern coral reefs support approximately 830 reef-building scleractinian coral species and an estimated one to nine million total reef-associated species including fishes (over 4 000 reef-associated species), molluscs, crustaceans, echinoderms, polychaetes, algae, and microbial communities making reefs the most biodiverse marine ecosystems on the planet.[3,7] Structural diversity among corals is substantial: branching Acropora species form the high-relief thickets characteristic of healthy Indo-Pacific reefs, massive Porites species build domed colonies capable of reaching many metres in diameter over centuries of growth, plating Montipora species maximise photosynthetic surface area in deeper light-limited environments, and encrusting species bind the carbonate framework. This morphological diversity creates the three-dimensional habitat complexity that supports reef-associated fauna across size classes and ecological roles.

Reef zonation from the shallow reef flat through the reef crest to the fore-reef slope and deeper mesophotic zones reflects gradients of light availability, wave energy, sediment deposition, and thermal exposure. The shallow reef flat experiences highest light but also highest temperature and desiccation stress at low tides; the reef crest absorbs the strongest wave energy and is dominated by robust, structurally resistant species; the fore-reef slope hosts the greatest structural and species diversity; mesophotic reefs (30–150 m depth) support distinct communities and may serve as thermal refugia and sources of larval recruitment to damaged shallow reefs.

Coral–algal symbiosis is obligate for most reef-building corals. The endosymbiotic dinoflagellates of the family Symbiodiniaceae (formerly classified as the single genus Symbiodinium) were reclassified by LaJeunesse and colleagues in 2018 into seven genera: Symbiodinium, Breviolum, Cladocopium, Durusdinium, Effrenium, Fugacium, and Gerakladium.[4] These genera differ substantially in thermal tolerance, photosynthetic efficiency, and nutrient transfer to the host. Cladocopium is the most widespread in Indo-Pacific corals but is thermally sensitive; Durusdinium (clade D) is thermally more tolerant but provides less carbohydrate to the host and associates with slower coral growth. Host–symbiont specificity varies widely, from strict vertical transmission of a single clade in some brooders to flexible horizontal acquisition of multiple clades in broadcast spawners. Coral-associated microbiomes (bacteria, archaea, viruses) further modulate holobiont function and are increasingly recognised as components of the coral immune and metabolic system.[5]

3. MECHANISMS OF THERMAL BLEACHING

Bleaching is an acute response to environmental stress, most commonly thermal stress exceeding the local long-term summer maximum by approximately 1°C for extended periods. The degree-heating-weeks (DHW) metric, developed by NOAA's Coral Reef Watch programme, quantifies accumulated thermal stress by integrating the number of weeks that sea-surface temperature has exceeded a defined bleaching threshold. Values above 4 DHW typically trigger observable bleaching and values above 8 DHW cause significant mortality.[8] Satellite-derived DHW products now provide near-real-time global monitoring and forecast fields that inform reef-management responses, including temporary closures of stressed reefs to diving and fishing.

At the cellular level, heat stress damages photosystem II in Symbiodiniaceae, reducing photosynthetic efficiency and producing reactive oxygen species (ROS) including superoxide radicals, hydrogen peroxide, and hydroxyl radicals. ROS diffuse across symbiont membranes into the coral host, overwhelming antioxidant defences (superoxide dismutase, catalase, glutathione peroxidase) and damaging host tissues. The breakdown of the symbiosis proceeds through several possible pathways: the host may exocytose symbiont-containing vesicles, digest symbionts via autophagy or apoptosis, or the symbionts themselves may leave the host in response to intracellular stress cues. Ultraviolet radiation, elevated salinity variation, and nutrient imbalance can independently or synergistically trigger bleaching, but thermal stress is by far the dominant cause of mass-bleaching events.

Coral species vary widely in thermal tolerance. Branching Acropora and Pocillopora species are generally among the most thermally sensitive, while massive Porites species, faviids, and siderastreids are typically more thermally tolerant. Intraspecific variation is also substantial, determined by a combination of host genetics, symbiont clade identity, and acclimation history. Corals hosting thermally tolerant Durusdinium (formerly Symbiodinium clade D) symbionts bleach less readily than those hosting sensitive Cladocopium clades,

though Durusdinium associations often entail fitness trade-offs including slower growth and reduced reproductive output. Prolonged loss of symbionts starves the coral which cannot meet energetic demands from heterotrophic feeding alone in most species and can lead to tissue death within weeks. Mortality after bleaching depends on the duration and severity of thermal stress, compounding biotic stressors (disease, predation), and the availability of refugia for larval recruitment during recovery.

Fig 1: Tropical sea-surface-temperature anomalies 1980–2024. Vertical dotted lines mark documented mass-bleaching years.[1,2,6]

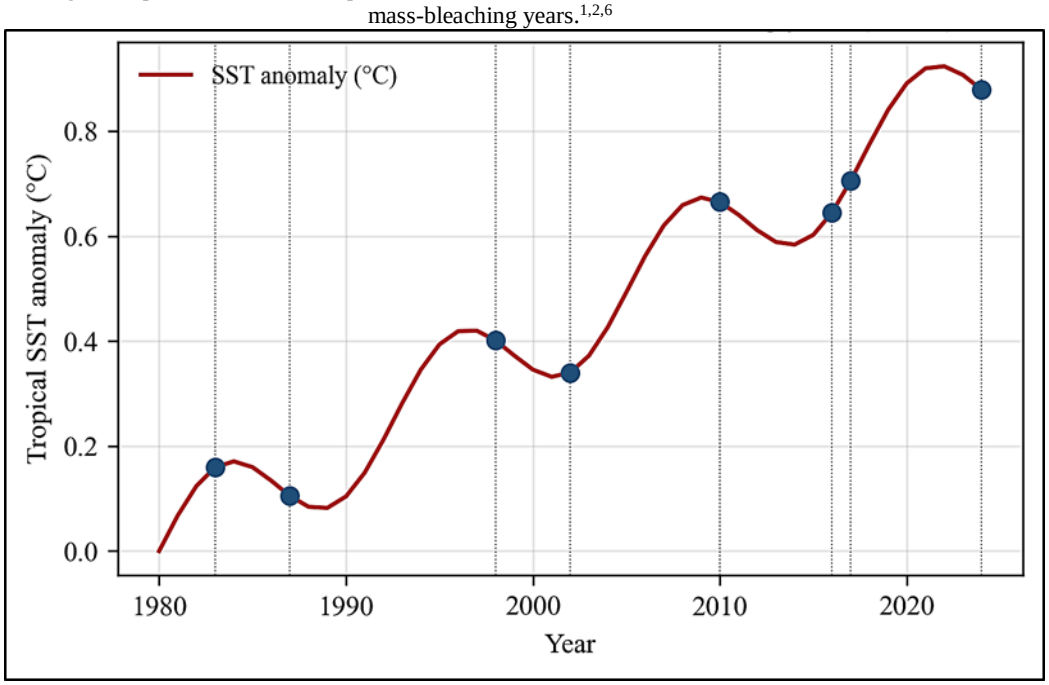

4. GLOBAL BLEACHING RECORD AND REGIONAL IMPACTS

Five global bleaching events have been declared: 1983, 1987, 1998, 2010, and 2014–2017, with a fifth announced in 2023.[1,2,6] The 2016–2017 back-to-back bleaching on the Great Barrier Reef killed roughly 50 percent of shallow-water corals in the northern sector.[9] The Caribbean has experienced long-term coral-cover declines exceeding 50 percent since the 1980s, driven by a combination of thermal stress, disease, and compounding anthropogenic pressures.[10] Figure 2 summarises regional changes in live coral cover between 1998 and 2017.

Fig 2: Mean live-coral cover by region in 1998 vs 2017 (data summarised from GCRMN global monitoring).[1,10]

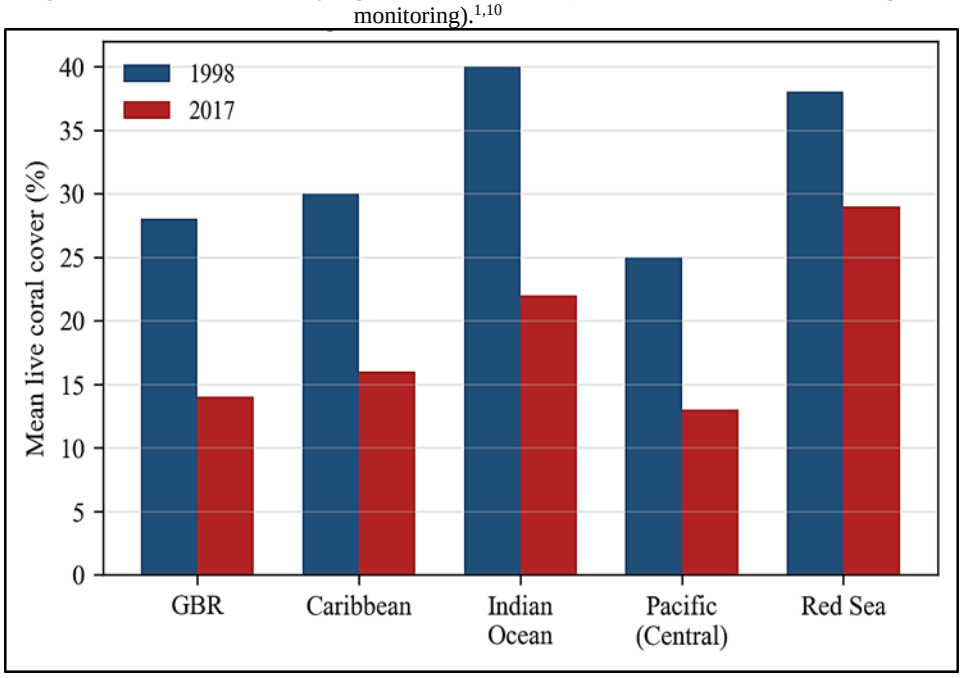

Table 1. Major documented global-scale coral-bleaching events. [1,2,6]

Event	Years	Climate driver	Approximate global impact
First global	1983	El Niño (mild)	Caribbean and Pacific patches
Second global	1987	El Niño	Caribbean-wide reports
Third global	1998	Strong El Niño	~16 % of world's corals dying
Fourth global	2010	Moderate El Niño + NH warm summer	Widespread IWP + Caribbean
2014–2017	2014–17	Very strong El Niño (2015–16)	75 % of reefs affected; GBR mass mortality
2023–ongoing	2023–present	Marine heatwaves + anthropogenic SST	Fifth global event declared by NOAA

5. ADAPTATION, ACCLIMATION, AND ASSISTED EVOLUTION

Coral thermal tolerance shows genetic variation both among and within species. Populations chronically exposed to high variability in thermal regime for example reef flats in the Persian/Arabian Gulf, where summer temperatures routinely exceed 34 °C exhibit thermal tolerances up to 4 °C above those of conspecifics in thermally stable environments. This evidence of local adaptation motivates interventions that identify, protect, and propagate thermally resilient genetic stock.

Symbiont shuffling replacement of thermally sensitive Cladocopium clades with more tolerant Durusdinium has been documented after bleaching events and may confer short-term heat tolerance at the cost of reduced calcification rates and slower coral growth.[4] Shuffling can occur within weeks following thermal stress, but the resulting symbiosis is often less stable and reverts to the original symbiont community over months when thermal conditions normalise. Horizontal transmission of heat-tolerant Symbiodiniaceae, laboratory selection of thermally robust strains, and engineered Durusdinium lineages are active experimental avenues.

Assisted evolution strategies proposed by van Oppen and colleagues encompass several complementary approaches. Selective breeding mates individuals that survived bleaching to enhance heat-tolerance heritability in progeny. Laboratory evolution of Symbiodiniaceae under incremental thermal stress selects for tolerant strains that can be reintroduced to host corals. Coral probiotics and microbiome engineering aim to manipulate associated bacterial communities that influence coral immunity and stress response.[11] Cross-species hybridisation between thermally sensitive and tolerant congeners has produced viable heat-tolerant hybrids in the laboratory, though ecological and evolutionary implications of hybrid introduction remain controversial. While all these approaches show promise at reef-scale demonstration, scaling to ocean-basin protection remains unproven, and timescales of thermal-tolerance enhancement via assisted evolution are uncertain relative to the pace of warming.

6. CONSERVATION STRATEGIES AND OCEAN ACIDIFICATION

Three categories of conservation intervention are established. First, reduction of local stressors: water-quality improvement through reduced agricultural runoff and sewage discharge, overfishing control that preserves herbivorous fishes grazing algae off reefs, and limits on coastal development reduce compounding pressure on corals and support post-bleaching recovery.[12] Evidence from the Great Barrier Reef and the Florida Keys suggests that local-pressure reduction can measurably improve reef resilience to thermal stress, extending the thermal-stress window that reefs can absorb before entering collapse trajectories.

Second, marine-protected-area (MPA) networks based on functional connectivity and refugia from thermal stress have been implemented in the Coral Triangle, the Western Indian Ocean, and the Caribbean.[13] Effective MPA networks combine strict no-take zones, multiple-use buffer areas, and scientifically informed spatial design that ensures larval connectivity between reef patches. Recent 'climate-smart' MPA design prioritises known thermal refugia deep reefs, upwelling zones, mesophotic reefs that may serve as sources for post-bleaching recolonisation.

Third, active restoration coral gardening (nursery-reared fragments planted onto degraded reefs), larval propagation (collecting and settling coral spawn at scale), microfragmentation (dividing corals into small fragments to accelerate growth), and 3D-printed reef structures has demonstrated efficacy at local scales.[14] Coral Restoration Foundation, SECORE International, and Reef Restoration Foundation have restored tens of thousands of corals across the Caribbean and Indo-Pacific, though the spatial scale relative to total reef area remains very small.

Beyond thermal stress, ocean acidification poses a second climate-driven threat. Atmospheric CO_2 dissolving in seawater reduces pH and aragonite saturation, slowing coral calcification. By 2100 under high-emission scenarios, aragonite saturation states over most tropical seas are projected to fall below values at which net reef accretion can be sustained. Combined effects of warming and acidification are non-linear and often synergistic. Ultimately, long-term reef persistence depends on atmospheric CO_2 stabilisation within the 1.5–2 °C warming range specified by the Paris Agreement; conservation interventions can extend the transition window but cannot substitute for global mitigation.

7. SOCIO-ECONOMIC IMPLICATIONS AND COUPLED HUMAN–REEF SYSTEMS

The implications of coral-reef decline extend substantially beyond biological biodiversity to the well-being of reef-dependent human communities. An estimated 500 million people derive food, livelihood, or income directly from reef fisheries and associated activities. Small Island Developing States in the Pacific, Caribbean, and Indian Ocean depend on reef fisheries for 60–90 per cent of animal protein in coastal communities. Tourism generates substantial employment and foreign-exchange earnings in reef-dependent economies including Australia, the Maldives, Egypt, and the Caribbean states; the Great Barrier Reef alone contributes approximately AU$6 billion annually to the Australian economy and supports 64 000 jobs. Coastal protection from reef dissipation of wave energy is estimated to prevent billions of dollars per year in property damage globally; without reef barriers, coastal erosion and storm damage would increase sharply, with disproportionate impact on low-income coastal populations.

Reef decline therefore produces cascading socio-economic shocks. Subsistence fisheries targeting reef species show declining catches per unit effort across the Coral Triangle, Caribbean, and Indian Ocean, pushing fishers toward less sustainable practices (dynamite, cyanide) and non-selective gear. Dive tourism revenue has collapsed on severely bleached reefs (Maldives, parts of the Great Barrier Reef), requiring substantial adaptive-management responses. Climate-displacement pressures on low-lying coastal populations are amplified by reduction of coastal-protection services. International climate-adaptation finance, including Green Climate Fund and Loss and Damage Fund mechanisms, has begun to incorporate reef-ecosystem concerns alongside conventional infrastructure and agriculture interventions.

Integrated reef-management frameworks increasingly couple ecological, social, and economic considerations. Community-based resource management, locally managed marine areas (LMMAs) particularly prominent in Fiji and other Pacific states, and co-management arrangements between government fisheries agencies and traditional coastal communities have been associated with improved reef outcomes. Payment-for-ecosystem-services schemes, reef insurance (pioneered in Mexico for Quintana Roo), and blue-bond financing represent emerging financial instruments for reef protection.

8. CONCLUSION

Coral reefs are among the ecosystems most immediately threatened by climate change. Mass bleaching has transitioned from a rare phenomenon into a recurrent ecological disturbance, reshaping reef communities toward weedy, smaller-bodied coral assemblages with reduced structural complexity, diminished habitat provision for reef-associated fauna, and reduced capacity to provide ecosystem services on which human communities depend.[1,9] The scientific evidence base is now mature: the mechanisms of thermal bleaching, the trajectory of mass-bleaching events, the limits of assisted-evolution interventions, and the economic scale of reef-dependence are all well characterised. Meaningful conservation requires convergent action on three fronts: global climate mitigation to stabilise greenhouse-gas concentrations, local stressor reduction to strengthen reef resilience, and strategic restoration and assisted-evolution interventions to bridge the biological response to ongoing thermal change. The fate of reef biodiversity and of the human communities that depend on it will largely be determined within the next three decades. The scientific tools, conservation techniques, and policy frameworks now exist; what remains is the political and financial commitment to deploy them at the scale required.

REFERENCES

1. Hughes TP, Kerry JT, Álvarez-Noriega M, et al. 2017. Global warming and recurrent mass bleaching of corals. *Nature*. 543(7645):373–377.
2. Eakin CM, Morgan JA, Heron SF, et al. 2010. Caribbean corals in crisis: record thermal stress, bleaching, and mortality in 2005. *PLoS ONE*. 5(11):e13969.
3. Hoegh-Guldberg O, Mumby PJ, Hooten AJ, et al. 2007. Coral reefs under rapid climate change and ocean acidification. *Science*. 318(5857):1737–1742.
4. LaJeunesse TC, Parkinson JE, Gabrielson PW, et al. 2018. Systematic revision of Symbiodiniaceae highlights the antiquity and diversity of coral endosymbionts. *Current Biology*. 28(16):2570–2580.
5. Muscatine L, Porter JW. 1977. Reef corals: mutualistic symbioses adapted to nutrient-poor environments. *BioScience*. 27(7):454–460.

6. Heron SF, Maynard JA, van Hooidonk R, Eakin CM. 2016. Warming trends and bleaching stress of the world's coral reefs 1985–2012. *Scientific Reports*. 6:38402.
7. Fisher R, O'Leary RA, Low-Choy S, et al. 2015. Species richness on coral reefs and the pursuit of convergent global estimates. *Current Biology*. 25(4):500–505.
8. Liu G, Heron SF, Eakin CM, et al. 2014. Reef-scale thermal stress monitoring of coral ecosystems: new 5-km global products from NOAA Coral Reef Watch. *Remote Sensing*. 6(11):11579–11606.
9. Hughes TP, Kerry JT, Baird AH, et al. 2018. Global warming transforms coral reef assemblages. *Nature*. 556(7702):492–496.
10. Jackson JBC, Donovan MK, Cramer KL, Lam VV. 2014. *Status and trends of Caribbean coral reefs: 1970–2012*. Gland (Switzerland): IUCN.
11. van Oppen MJH, Gates RD, Blackall LL, et al. 2017. Shifting paradigms in restoration of the world's coral reefs. *Global Change Biology*. 23(9):3437–3448.
12. Mumby PJ, Steneck RS. 2008. Coral reef management and conservation in light of rapidly evolving ecological paradigms. *Trends in Ecology & Evolution*. 23(10):555–563.
13. Beyer HL, Kennedy EV, Beger M, et al. 2018. Risk-sensitive planning for conserving coral reefs under rapid climate change. *Conservation Letters*. 11(6):e12587.
14. Boström-Einarsson L, Babcock RC, Bayraktarov E, et al. 2020. Coral restoration—a systematic review of current methods, successes, failures and future directions. *PLoS ONE*. 15(1):e0226631.

INTERNATIONAL JOURNAL OF PURE SCIENCE RESEARCH STUDIES (IJPSRS)
(Open Access, Double-Blind Peer Reviewed Journal)
ISSN Online: ISSN Print
EDU SCHOOL
ijpsrs.com

Graph Neural Networks: Mathematical Foundations and Algorithmic Frameworks

Lejo J Manavalan

Assistant Professor and Research Guide, Department of Mathematics, Little Flower College, Guruvayur, India

Article Information

Received: 3rd February 2026
Received in revised form: 5th March 2026
Accepted: 7th April 2026
Available online: 14th May 2026

Volume: 2
Issue: 2
DOI: https://doi.org/10.5281/zenodo.20151052

Abstract

Graph neural networks (GNNs) extend deep learning to data supported on graph-structured domains. Motivated by problems in chemistry, social networks, recommender systems and relational reasoning, GNN architectures have matured into a rigorous subfield combining graph theory, spectral analysis and approximation theory. This paper offers a mathematical review of GNN foundations. We begin with spectral formulations based on the graph Laplacian, derive the message-passing neural network framework, and survey expressive-power results including the equivalence of 1-WL colour refinement and standard message-passing. Representative architectures GCN, GraphSAGE, GAT, and GIN are compared on citation-network benchmarks. The paper closes with a discussion of over-smoothing, long-range dependency, and recent higher-order extensions.

Keywords: Graph Neural Network, Message Passing, Spectral Graph Theory, Graph Convolution, Weisfeiler-Leman.

1. INTRODUCTION

Many datasets of contemporary scientific and commercial interest have intrinsic graph structure. Molecules are graphs with atoms as nodes and bonds as edges. Citation networks link papers by their references. Social graphs encode friendships, follower relations, and communication. Knowledge graphs encode entity-relation triples capturing world knowledge. Protein interaction networks, transportation networks, recommender interaction graphs, and program dependency graphs all share this relational structure. Conventional convolutional and recurrent deep-learning architectures exploit grid or sequence regularities shift-equivariance for images, temporal recurrence for sequences that are unavailable in general graph data. Graph neural networks (GNNs) generalise convolution to arbitrary graphs by exchanging information along edges, enabling feature learning on relational data.[1,2]

GNNs emerged from two converging lines of development. The first was spectral graph signal processing, which generalises Fourier analysis to functions on graphs via the graph Laplacian spectrum; the second was the early neural-network work on structured prediction (recursive neural networks, neural networks for graphs by Scarselli and colleagues in 2009).[3] The modern GNN era began with the work of Bruna and colleagues on spectral graph convolutions in 2013, the localised Chebyshev-polynomial approximation of Defferrard and colleagues in 2016, and the highly influential simplified graph convolutional network of Kipf and Welling in 2017.[6] Since then the field has expanded dramatically, supporting a principled theory of expressiveness, convergence, and generalisation, together with a wide practical toolkit and substantial industry adoption.

This paper surveys the mathematical foundations, dominant architectural frameworks, and open problems of graph neural networks. Section 2 reviews spectral graph theory and its relationship to graph convolution. Section 3 presents the message-passing framework that unifies most modern architectures. Section 4 surveys

representative architectures. Section 5 addresses expressiveness results, particularly the equivalence of standard message-passing to the 1-dimensional Weisfeiler–Leman test. Section 6 presents empirical comparisons, and Sections 7–8 discuss challenges and conclusions.

2. GRAPH THEORY AND SPECTRAL FOUNDATIONS

Let G = (V, E) be an undirected graph with |V| = N vertices and |E| edges, adjacency matrix :

$$A \in \{0,1\}^{N\times N}\ A_{ij} = 1 \tag{1}$$

if ij ∈ E, else 0), degree matrix D = diag(d_1,…, d_N) where:

$$d_i = \sum_j A_{ij} \tag{2}$$

and combinatorial Laplacian L = D − A. The combinatorial Laplacian is symmetric positive semi-definite; its multiplicity of the zero eigenvalue equals the number of connected components, and its second-smallest eigenvalue (the Fiedler value) measures algebraic connectivity.

The normalised Laplacian $\hat{L} = I - D^{-1/2}AD^{-1/2}$ has eigenvalues in [0,2]; its eigenvectors $\{u_k\}$ and eigenvalues $\{\lambda_k\}$ provide a Fourier basis for graph signals $x \in \mathbb{R}^N$, with the graph Fourier transform $\hat{x} = U^T x$ and its inverse $x = U\hat{x}_3$. This construction generalises the classical Fourier transform: on the discrete circle Z/N with its cycle-graph Laplacian, the eigenvectors of L reduce to the classical discrete Fourier basis. Graph signal-processing concepts filtering, frequency bands, smoothness, multi-resolution analysis translate to arbitrary graphs via this spectral decomposition.

A graph convolution is defined by element-wise multiplication of spectral representations:

$$y = Ug_\theta(\Lambda)U^T x \tag{3}$$

where U is the eigenbasis, Λ = diag(λ_1,…, λ_N) , and g_θ a learnable filter function. Direct spectral evaluation requires $O(N^3)$ eigendecomposition and is non-transferable across graphs of different size. Localised filters admit polynomial parametrisations:

$$g_\theta(\Lambda) = \sum_k \theta_k T_k(\tilde{\Lambda}) \tag{4}$$

where T_k are Chebyshev polynomials and $\tilde{\Lambda}$ is a rescaled Laplacian, yielding O(|E|) complexity per evaluation and K-hop spatial locality for a polynomial of degree K[6]. The first-order Chebyshev approximation, augmented with renormalisation, yields the popular Graph Convolutional Network (GCN) layer. ChebNet with higher-order polynomials enjoys stronger expressive power at the cost of slightly higher per-layer compute, and has proven effective on tasks where longer-range dependencies matter.

Spectral analysis also provides theoretical tools for studying GNN properties. The spectral radius of the aggregation operator governs the stability of deep architectures; spectral smoothness of signals captures homophily (the tendency of connected nodes to share labels); and the interplay between graph spectrum and filter design explains phenomena such as over-smoothing and over-squashing that emerge in deep GNNs. The spectral perspective is complementary to the spatial (message-passing) view developed in the following sections.

3. MESSAGE PASSING FRAMEWORK

Gilmer and colleagues in 2017 introduced the unifying message-passing neural network (MPNN) framework that subsumes most contemporary graph neural architectures.[4] At layer l, each node v updates its representation $h_v^{(l)}$ via messages:

$$m_v = AGG(\{M(h_v, h_u, e_{uv}) | u \in N(v)\}) \tag{5}$$

followed by an update:

$$h_v^{(1+1)} = \dot{U}\left(h_v^{(1)}, m_v\right) \tag{6}$$

The aggregation AGG is a permutation-invariant function (sum, mean, max, attention-weighted, set-theoretic), ensuring that the output is independent of the arbitrary ordering of neighbours. M is a learnable message function (often a multi-layer perceptron or a linear transformation of concatenated features), and U is a learnable update function (typically a gated recurrent unit, multi-layer perceptron, or simple addition followed by nonlinearity).

The design of AGG, M, and U determines the expressive capacity and computational profile of the architecture. Sum aggregation, combined with injective update, yields maximally expressive message passing. Mean aggregation is appropriate when absolute neighbour count is irrelevant (common in citation networks). Max aggregation emphasises the most prominent neighbour feature. Attention-weighted aggregation adaptively

weights neighbours according to learned relevance. Set-theoretic aggregators (DeepSets, PNA) combine multiple aggregation strategies to capture richer neighbourhood distributions. Beyond single-step aggregation, iterative message passing stacks L layers, giving each node access to L-hop neighbourhood information.

Readout operations convert node representations to graph-level predictions. Standard choices are sum-, mean-, or max-pooling over node features; attention-based pooling (Set2Set, GMP) and hierarchical pooling (DiffPool, Top-k pooling, SAGPool) enable richer graph-level representations. The full MPNN framework is shown schematically in Figure 1, with node v receiving messages from each neighbour, aggregating them, and updating its own representation.

Fig 1: Message passing: at each layer a node v aggregates transformed features from its neighbourhood N(v) and updates its embedding.[4]

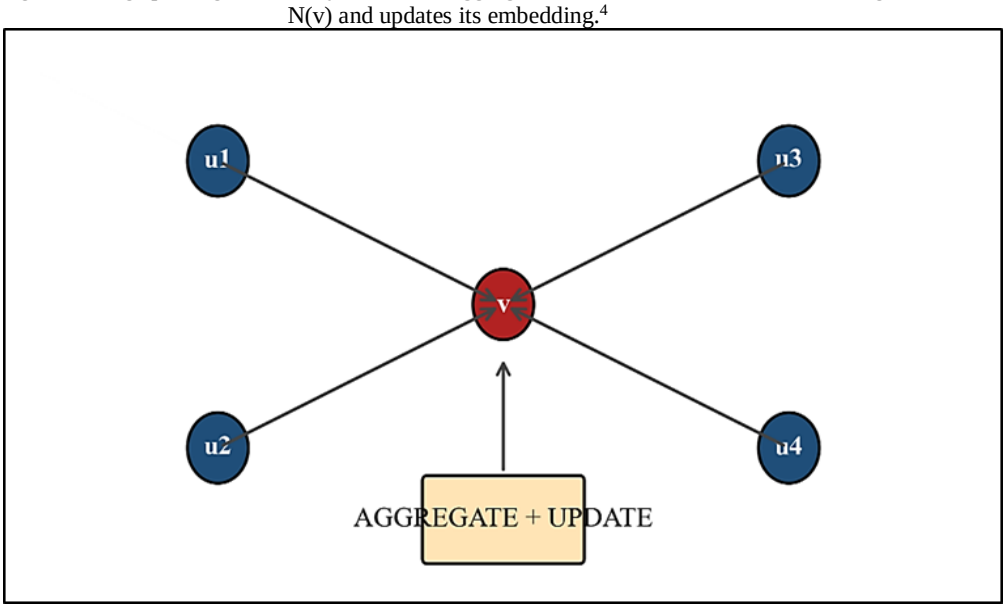

4. REPRESENTATIVE ARCHITECTURES

The Graph Convolutional Network (GCN) of Kipf and Welling uses first-order spectral approximations, giving a layer-wise propagation rule:

$$H^{(l+1)} = \sigma(\tilde{A}H^{(l)}W^{(l)} \tag{7}$$

with:

$$\tilde{A} = \tilde{D}^{-1/2}(A + I)\tilde{D}^{-1/2} \tag{8}$$

where I is added to preserve self-information via self-loops.[6] This renormalisation trick stabilises training and provides a simple yet effective baseline that has become the de facto standard entry point for graph-based deep learning. The GCN propagation can be interpreted as smoothing signals over the graph Laplacian's low-frequency components, consistent with the homophily assumption underlying many benchmark graph tasks.

GraphSAGE (SAmple and aggreGatE), introduced by Hamilton and colleagues, generalises the GCN framework with support for inductive learning on large or evolving graphs.[7] GraphSAGE samples fixed-size neighbourhoods (typically 10–25 neighbours per node), applies aggregator functions (mean, pooling, or LSTM), and concatenates with self-features. Neighbour sampling bounds per-node computation, enabling training on graphs with billions of edges via minibatch gradient descent. GraphSAGE has been deployed in production recommender systems at major technology companies including Pinterest and Uber.

The Graph Attention Network (GAT) replaces uniform aggregation with attention coefficients learned between neighbours, providing adaptive weighting that emphasises informative neighbours.[8] Each neighbour's contribution is weighted by a learned attention score:

$$\alpha_{ij} = \mathrm{softmax}_j\left(\mathrm{LeakyReLU}\left(a^T\left[Wh_i \parallel Wh_j\right]\right)\right) \tag{9}$$

where W is a shared linear transformation and a is an attention vector. Multi-head attention averages or concatenates outputs from multiple parallel attention computations, further improving expressiveness. GAT is particularly effective on heterophilic graphs where connected nodes may carry different labels.

The Graph Isomorphism Network (GIN) uses sum aggregation with a multi-layer perceptron update:

$$h_v^{(l+1)} = \mathrm{MLP}^{(l)}\left((1 + \epsilon^{(l)})\, h_v^{(l)} + \sum_{u \in N(v)} h_u^{(l)}\right) \tag{10}$$

Xu and colleagues showed that this formulation is as expressive as the 1-dimensional Weisfeiler–Leman graph-isomorphism test, the strongest possible for message-passing architectures[5]. GIN achieves strong performance on graph-level tasks including molecular property prediction on the ogbg-molhiv and QM9 benchmarks. Additional architectures include APPNP (personalised PageRank propagation), MixHop (mixing different hop neighbourhoods), GCNII (residual connections to avoid over-smoothing), and GraphTransformer (self-attention with structural encoding). Heterogeneous graph neural networks (R-GCN, HAN, HGT) handle graphs with multiple node and edge types, essential for knowledge graphs and multi-modal relational data.

5. EXPRESSIVE POWER AND WEISFEILER–LEMAN EQUIVALENCE

Xu and colleagues established a fundamental connection between message-passing GNNs and the 1-dimensional Weisfeiler–Leman (1-WL) graph-isomorphism test[5]. The 1-WL test iteratively refines node labels by hashing each node's current label together with the multiset of its neighbours' labels; two graphs are declared potentially isomorphic if their final label multisets match. Standard message-passing GNNs execute the same structural procedure with learned hash functions, and therefore cannot distinguish non-isomorphic graphs that 1-WL cannot distinguish. The Graph Isomorphism Network achieves the maximum expressiveness in this class under sum aggregation and injective update functions.

The 1-WL test is strictly weaker than graph isomorphism: classical counterexamples include pairs of k-regular graphs that are not isomorphic but share identical 1-WL refinements. To overcome this expressiveness ceiling, several higher-order architectures have been proposed.[9] k-WL inspired architectures operate on ordered k-tuples of nodes, attaining the stronger k-dimensional Weisfeiler–Leman test's expressive power at a computational cost exponential in k. Subgraph GNNs compute node representations by aggregating over multiple subgraphs rooted at each node, typically achieving expressive power between 2-WL and 3-WL while remaining computationally tractable. Simplicial and cell-complex networks generalise the message-passing framework to higher-dimensional algebraic-topological structures, naturally encoding triangles, cycles, and higher-order interactions. Graph transformers drop the strict locality constraint, using self-attention across all node pairs with structural positional encodings (Laplacian eigenvectors, random-walk features) to preserve graph structure information. Each of these approaches balances expressive power, computational cost, and empirical effectiveness differently; choice depends on application and scale.

6. EMPIRICAL COMPARISON

Figure 2 shows test accuracies of representative architectures on the Cora, Citeseer, and Pubmed citation benchmarks. Architectures with adaptive aggregation (GAT) and maximally expressive aggregation (GIN) tend to outperform simpler GCN on small graphs but converge on larger graphs. Personal-PageRank-based APPNP variants balance expressiveness with computational efficiency.[10] Table 1 summarises principal architectural tradeoffs.

Fig 2: Test accuracy on standard citation benchmarks for representative GNN architectures.[5,6,7,8,10]

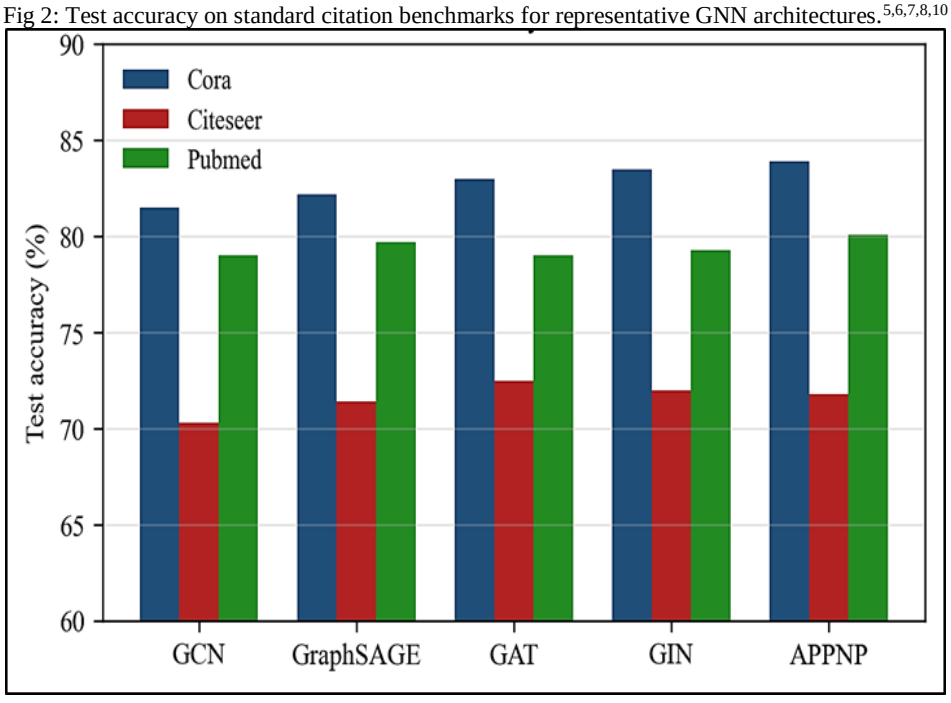

Table 1. Architectural comparison of representative GNNs. [5,6,7,8,10]

Architecture	Aggregation	Spectral/Spatial	Key property
GCN	Symmetric-normalised mean	Spectral (Chebyshev order 1)	Simple, scalable baseline
GraphSAGE	Mean / pool / LSTM	Spatial sampling	Inductive on large graphs
GAT	Attention-weighted sum	Spatial	Adaptive neighbour weighting
GIN	Injective sum + MLP	Spatial	1-WL expressive
APPNP	Personalised PageRank	Propagation	Decouples depth from expressiveness

7. CHALLENGES AND FUTURE DIRECTIONS

Several challenges continue to structure the research agenda. First, over-smoothing: deep GNNs collapse node representations as layers increase, so that nodes within a connected component converge to identical embeddings.[11] Mathematically, this occurs because repeated graph-convolution operations are analogous to repeatedly applying a low-pass filter, eventually projecting signals onto the Laplacian's null space. Residual connections (GCNII), skip connections, PairNorm normalisation, personalised-PageRank propagation (APPNP), and spectral regularisers mitigate over-smoothing, enabling effective networks of 20+ layers on some benchmarks.

Second, over-squashing and long-range dependency: message-passing restricts information flow to local neighbourhoods, so information from nodes many hops away is exponentially compressed through intermediate aggregation an effect termed 'over-squashing' by Topping and colleagues. Graph rewiring techniques, graph curvature-guided adjustment, and the insertion of virtual global nodes have been proposed as remedies. Graph transformers and higher-order architectures address long-range dependency by breaking the strict locality of message-passing,[9] though at higher computational cost and with less-developed theory.

Third, generalisation theory for GNNs on graphs drawn from complex distributions provides a growing mathematical foundation. The 'graphon' limit treating large graphs as samples from a continuous kernel enables transferability results establishing that GNNs trained on moderate-sized graphs generalise predictably to larger graphs of similar structure.[12] PAC-Bayesian bounds, Rademacher complexity analyses, and neural-tangent-kernel results are advancing the theoretical understanding of generalisation, overparameterisation, and implicit regularisation in GNNs.

Fourth, scalability remains an engineering challenge. Techniques including neighbour sampling, layer-wise sampling, historical embeddings (GraphSAINT, Cluster-GCN), distributed training across partitioned graphs, and GPU-optimised sparse operations have enabled training on graphs with billions of nodes. Frameworks such as DGL, PyTorch Geometric, and JAX-based Jraph continue to reduce the engineering cost of large-scale GNN deployment. Fifth, robustness and explainability: GNNs are sensitive to adversarial perturbations of graph structure, and explanations of GNN predictions require methods tailored to relational data (GNNExplainer, PGExplainer, subgraph-level interpretability). Research in these directions is expanding rapidly alongside the broader deep-learning interpretability literature.

8. APPLICATIONS ACROSS DOMAINS

GNN applications span diverse scientific and industrial domains. In chemistry and drug discovery, GNNs predict molecular properties (QM9, MoleculeNet benchmarks), generate molecular structures via graph generative models, and model chemical reactions. AlphaFold's initial protein-structure predictions used graph-attention components; AlphaFold-Multimer and more recent derivatives continue to integrate graph architectures. In materials science, GNNs predict formation energies, band gaps, and phonon spectra of crystalline materials, with dedicated crystal-graph architectures (CGCNN, MEGNet, ALIGNN) achieving state-of-the-art accuracy on materials datasets.

In recommender systems, GNNs represent user item interactions as bipartite graphs and leverage message passing for collaborative filtering. PinSage at Pinterest, LightGCN, and Uber's graph-based recommenders are production deployments operating on graphs with billions of edges. In social-network analysis, GNNs predict user influence, community structure, and content diffusion. In knowledge-graph completion, relational GCNs and knowledge-graph embedding methods predict missing triples in Freebase, WordNet, and domain-specific knowledge graphs.

In physics and engineering, GNNs model particle physics (jet tagging, event reconstruction at ATLAS and CMS), fluid dynamics (mesh-based GNN simulators such as DeepMind's MeshGraphNet), rigid-body dynamics, and power-grid analysis. In transportation and logistics, GNNs predict traffic flow, route congestion,

and supply-chain disruption on road and transit networks. In finance, GNNs detect fraudulent transactions, estimate credit risk from transaction graphs, and model portfolio-risk dependencies.

9. CONCLUSION

Graph neural networks have matured into a principled methodology at the intersection of spectral graph theory, algebraic topology, and deep learning. Expressiveness, generalisation, and computational cost are each the subject of active theoretical progress, supported by a broad software ecosystem and large-scale empirical benchmarking. Empirical performance on citation, molecular, recommender, and knowledge-graph benchmarks continues to improve, and the mathematical tools developed for GNNs expressive-power hierarchies, spectral analysis, graphon limits are migrating into broader areas of relational machine learning. The field is now embedded in the broader geometric deep-learning programme, which systematically treats data with symmetry and structure across manifolds, grids, groups, graphs, and geodesics. Further progress will likely come from tighter integration with scientific domain knowledge (physics-informed architectures, causal inference), improved methods for heterogeneous and dynamic graphs, and robust foundations for large-scale deployment on graphs with billions of nodes.

REFERENCES

1. Bronstein MM, Bruna J, Cohen T, Veličković P. 2021. Geometric deep learning: grids, groups, graphs, geodesics, and gauges. arXiv. 2104.13478.
2. Hamilton WL. 2020. Graph representation learning. Synth Lect Artif Intell Mach Learn. 14(3):1–159.
3. Shuman DI, Narang SK, Frossard P, Ortega A, Vandergheynst P. 2013. The emerging field of signal processing on graphs. IEEE Signal Process Mag. 30(3):83–98.
4. Gilmer J, Schoenholz SS, Riley PF, Vinyals O, Dahl GE. 2017. Neural message passing for quantum chemistry. Proc Int Conf Mach Learn. 70:1263–1272.
5. Xu K, Hu W, Leskovec J, Jegelka S. 2019. How powerful are graph neural networks? Proc Int Conf Learn Represent.
6. Kipf TN, Welling M. 2017. Semi-supervised classification with graph convolutional networks. Proc Int Conf Learn Represent.
7. Hamilton WL, Ying R, Leskovec J. 2017. Inductive representation learning on large graphs. Proc Adv Neural Inf Process Syst. 30:1024–1034.
8. Veličković P, Cucurull G, Casanova A, Romero A, Liò P, Bengio Y. 2018. Graph attention networks. Proc Int Conf Learn Represent.
9. Morris C, Ritzert M, Fey M, et al. 2019. Weisfeiler and Leman go neural: higher-order graph neural networks. Proc AAAI Conf Artif Intell. 33(1):4602–4609.
10. Klicpera J, Bojchevski A, Günnemann S. 2019. Predict then propagate: graph neural networks meet personalized PageRank. Proc Int Conf Learn Represent.
11. Oono K, Suzuki T. 2020. Graph neural networks exponentially lose expressive power for node classification. Proc Int Conf Learn Represent.
12. Ruiz L, Gama F, Ribeiro A. 2020. Graphon neural networks and the transferability of graph neural networks. Proc Adv Neural Inf Process Syst. 33:1702–1712.

INTERNATIONAL JOURNAL OF PURE SCIENCE RESEARCH STUDIES (IJPSRS)
(Open Access, Double-Blind Peer Reviewed Journal)
ISSN Online: ISSN Print
EDU SCHOOL ijpsrs.com

Gravitational Wave Astronomy: Detection Methods and Astrophysical Implications

Sini R

Assistant Professor, Department Of Physics, Providence Women's College (Autonomous), Calicut, Kerala, India

*Kerala***Article Information**

Received: 5th February 2026
Received in revised form: 7th March 2026
Accepted: 8th April 2026
Available online: 14th May 2026

Volume: 2
Issue: 2
DOI: https://doi.org/10.5281/zenodo.20151550

Abstract

The direct detection of gravitational waves in September 2015 by the Advanced LIGO observatories opened a new observational window on the universe. In less than a decade the field has transitioned from a single detection to a catalogue of nearly a hundred compact-binary coalescences, together with the multi-messenger observation of a binary neutron-star merger in 2017 that simultaneously produced gravitational waves, electromagnetic emission, and kilonova signatures. This paper reviews the theoretical background of gravitational waves, the principles and performance of laser-interferometric detectors, the catalogue of significant detections, and the astrophysical implications for compact-object populations, tests of general relativity, cosmology, and the origin of heavy elements. Future detector generations LIGO Voyager, the Einstein Telescope, Cosmic Explorer, and the space-based LISA are expected to extend reach to high redshifts and to lower frequencies inaccessible to ground-based instruments.

Keywords: Gravitational Waves, LIGO, Multi-Messenger Astronomy, Compact Binary Coalescence, General Relativity, LISA.

1. INTRODUCTION

Gravitational waves were predicted by Einstein in 1916 as a consequence of the linearised field equations of general relativity.[3] In the weak-field limit the Einstein equations reduce to a wave equation propagating at the speed of light, with two polarisation modes traditionally labelled 'plus' and 'cross', corresponding to quadrupolar distortions of test-mass separations transverse to the propagation direction. For decades following Einstein's prediction, the physical reality of gravitational waves was disputed: even Einstein himself briefly believed in 1936 that the waves were coordinate artefacts, a view later reversed following theoretical work by Bondi, Pirani, and Feynman establishing their physical existence through the concept of energy transport by gravitational radiation.[1] The 'sticky bead' argument of Feynman and the Bondi news-function analysis established that gravitational waves must carry energy away from their sources and can perform work on matter.

The indirect evidence for gravitational-wave emission was provided by the Hulse Taylor binary pulsar PSR B1913+16, discovered in 1974. Continuous timing of this system over four decades revealed orbital decay consistent with general-relativistic emission of gravitational radiation to better than one per cent precision, earning Hulse and Taylor the 1993 Nobel Prize in Physics.[4] Subsequent binary-pulsar systems notably the double pulsar PSR J0737−3039 have extended these tests of the quadrupole formula and confirmed additional post-Newtonian effects. Nevertheless, direct detection of gravitational waves remained elusive because the intrinsic weakness of the gravitational interaction translates into strain amplitudes of order 10^{-21} at Earth from astrophysical sources, requiring kilometre-scale laser interferometers to resolve.

The first direct detection, GW150914, was announced in February 2016 following joint observation by the two LIGO detectors at Hanford and Livingston on 14 September 2015, during the first engineering run of the Advanced LIGO detectors.[1] GW150914 corresponded to the merger of two stellar-mass black holes of approximately 36 and 29 solar masses at a luminosity distance of approximately 410 Mpc (redshift $z \approx 0.09$); the coalescence produced a final 62-solar-mass black hole with three solar masses of energy radiated as gravitational waves, corresponding to a peak luminosity briefly exceeding the combined electromagnetic output of all stars in the observable universe. The discovery earned Weiss, Barish, and Thorne the 2017 Nobel Prize in Physics. In August 2017, the GW170817 binary neutron-star merger was observed in coincidence with a short gamma-ray burst (GRB 170817A) detected by Fermi GBM 1.7 s after the merger, and subsequent electromagnetic follow-up across radio, optical, X-ray, and ultraviolet bands identified the kilonova AT2017gfo in the galaxy NGC 4993, inaugurating multi-messenger gravitational-wave astronomy.[2] Spectroscopic analysis of the kilonova provided direct observational evidence for r-process nucleosynthesis of heavy elements, including gold, platinum and lanthanides, in compact-object mergers.

2. THEORETICAL BACKGROUND

In the weak-field limit the metric may be written as:

$$g_{\mu v} = \eta_{uv} + h_{\mu v} \text{ with } | h_{\mu v} | \ll 1 \quad (1)$$

where $\eta_{\mu v}$is the Minkowski metric and $h_{\mu v}$ a small perturbation. Imposing the Lorenz gauge $\partial_{\mu} \bar{h}^{uv} = 0$ on the trace-reversed perturbation:

$$\bar{h}_{\mu v} \equiv h_{\mu v} - \frac{1}{2}\eta_{\mu v} h \quad (2)$$

reduces the Einstein field equations to:

$$\Box \bar{h}_{\mu v} = -\frac{16\pi G}{C^4} T_{uv} \quad (3)$$

which in vacuum becomes a simple wave equation with solutions propagating at the speed of light.[3] The transverse-traceless (TT) gauge further restricts $h_{\mu v}$ to its physical two-polarisation content, explicitly exhibiting the quadrupolar 'plus' and 'cross' polarisation modes. Emission is governed by the quadrupole formula: the luminosity:

$$L = \frac{G}{5c^5} \langle \dddot{Q}_{ij} \ \dddot{Q}^{ij} \rangle \quad (4)$$

where $Q_{\{ij\}}$is the mass-quadrupole moment and the triple dot denotes the third time derivative. For a binary of chirp mass:

$$M_{chirp} = \frac{(m_1 m_2)^{3/5}}{(m_1 + m_2)^{1/5}} \quad (5)$$

the strain amplitude scales as:

$$h \propto \frac{\left(\frac{GM_C}{C^2}\right)^{5/3} \left(\frac{\pi f}{C}\right)^{2/3}}{D} \quad (6)$$

and the frequency evolves as:

$$\frac{df}{dt} \propto f^{11/3} \quad (7)$$

producing the characteristic chirp waveform (Figure 1). This phase evolution provides the principal observable for measuring the chirp mass, which is the best-constrained source parameter in compact-binary detections. Post-Newtonian expansions systematically include higher-order corrections in v/c; effective-one-body formalisms resum the post-Newtonian series into a one-body problem with modified Hamiltonian; and numerical-relativity simulations solve the full Einstein equations during merger. Together these techniques provide template banks used for matched-filter searches[5]. Inspiral, merger, and ringdown are modelled respectively by post-Newtonian expansions, full numerical relativity, and black-hole perturbation theory with quasi-normal modes; modern phenomenological and surrogate waveform families (IMRPhenom, SEOBNR, NRSur) integrate these regimes.

Direct detection is possible because the strain signal, though minute, is coherent and has a well-modelled waveform. Matched filtering cross-correlates the detector output with template waveforms parameterised by source physics; the signal-to-noise ratio accumulates coherently over the many cycles of the inspiral, allowing detection of signals whose peak strain lies well below the instantaneous noise floor. Interferometric detectors compare the round-trip light-travel times along two orthogonal arms; a passing gravitational wave alternately lengthens one arm while shortening the other, producing a phase shift at the photodetector that scales linearly with the strain amplitude. Because the detectors measure strain rather than energy, sensitivity degrades only as the luminosity distance (rather than the inverse-square law), giving gravitational-wave astronomy disproportionate reach compared with electromagnetic surveys of comparable aperture.

Fig 1: Illustrative chirp waveform for a compact-binary coalescence. Frequency and amplitude increase until merger.[1,5]

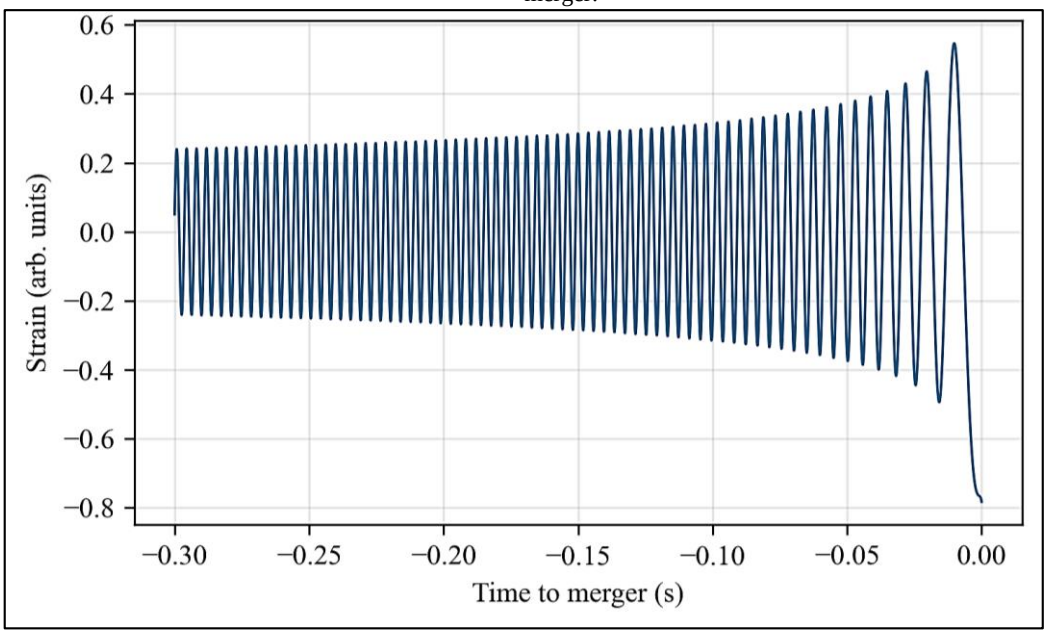

3. DETECTION METHODOLOGIES

The Advanced LIGO detectors use 4 km Fabry-Perot-enhanced Michelson interferometers with power and signal recycling, operating near quantum noise limits in the 100–1000 Hz band. Laser power of 100–200 kW circulates in each arm cavity (amplified from a 200 W input via power recycling), increasing the photon flux and consequently reducing shot noise. Signal recycling further tunes the frequency response. Test masses are 40 kg fused-silica mirrors suspended as quadruple pendulums providing seismic isolation in the detection band. Advanced Virgo (3 km arm length) in Italy and KAGRA (underground cryogenic, 3 km arm length, sapphire test masses cooled to 20 K) in Japan now operate as part of the international network.[1,6]

The design sensitivities are shown in Figure 2. At different frequencies distinct noise sources dominate: below 10 Hz the detectors are limited by seismic noise, residual mirror motion transmitted through the suspension chain, and Newtonian (gravity-gradient) noise from atmospheric and terrestrial mass movements that couple gravitationally to the test masses and cannot be shielded. Between 10 and 50 Hz, thermal noise in the test-mass coatings and in the suspension wires dominates; minimising thermal noise motivates cryogenic operation (implemented in KAGRA) and the development of crystalline or low-loss coating materials. Above ~100 Hz, quantum shot noise of the laser dominates; squeezed-light injection, in which vacuum fluctuations are 'squeezed' to redistribute uncertainty between conjugate variables, has been used to further reduce shot noise in the high-frequency band. Both LIGO and Virgo have operated with frequency-dependent squeezing since 2019, achieving 3–6 dB noise reduction in parts of the detection band.[7] Frequency-dependent squeezed-light filtering via a long filter cavity allows sensitivity improvement across the full detection band without sacrificing low-frequency performance.

Signal identification relies on matched-filter search pipelines that cross-correlate detector strain data against template banks of expected waveforms, typically containing 10^5 to 10^6 templates covering the astrophysically relevant parameter space in mass and spin. Coincident triggers across multiple detectors within light-travel-time windows establish candidate events, with background distributions estimated by time-sliding data streams to suppress accidental coincidences. Parameter estimation uses Bayesian inference with Markov-chain Monte Carlo or nested sampling to reconstruct the posterior distribution over source parameters (masses, spins, sky position, distance, inclination, polarisation). Low-latency pipelines such as GstLAL, MBTA, and PyCBC Live provide alerts to astronomical facilities within minutes to support electromagnetic follow-up, while offline deep analyses refine significance estimates and parameter measurements.

Fig 2: Design amplitude spectral density of the Advanced LIGO, Advanced Virgo and KAGRA detectors.[6,7]

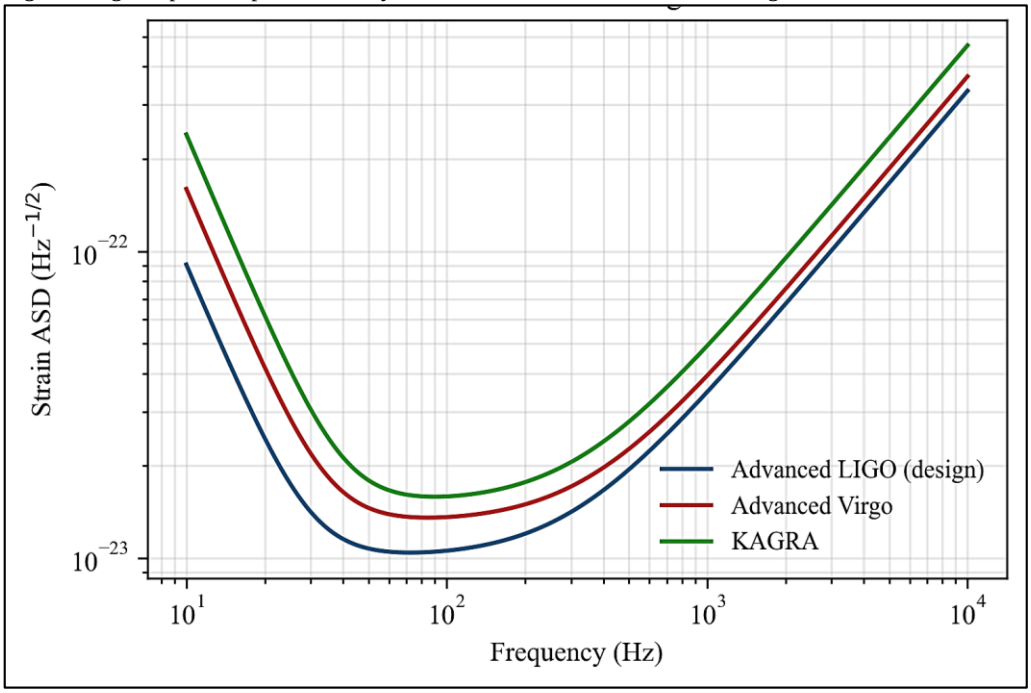

4. CATALOGUE OF EVENTS

The first three LIGO–Virgo observing runs produced the Gravitational-Wave Transient Catalogues GWTC-1 (first observing run, O1), GWTC-2 (O2 and first half of O3), and GWTC-3 (full O3), comprising approximately 90 significant compact-binary coalescence candidates.[8] The catalogue is dominated by binary black-hole (BBH) mergers with component masses ranging from approximately 5 to 85 solar masses. The BBH mass distribution exhibits rich structure: a primary peak near 35 solar masses consistent with the pulsational pair-instability mass gap, a secondary peak near 10 solar masses possibly reflecting compact-binary formation channels, and a rising tail toward low masses.

Several events merit specific mention. GW150914, the first detection, remains the most spectacular BBH event: two black holes of 36 and 29 solar masses coalescing at 410 Mpc produced a signal with signal-to-noise ratio of 24 and established the template for subsequent discoveries. GW170817, the first binary neutron-star (BNS) merger, detected on 17 August 2017, enabled the first multi-messenger gravitational-wave observation, with electromagnetic counterparts across radio through X-ray bands. The kilonova AT2017gfo provided the first direct spectroscopic evidence of r-process nucleosynthesis of heavy elements in compact-object mergers. GW170817 also provided the first measurement of the speed of gravitational waves to within 10^{-15} of c, and constrained the neutron-star equation of state through the tidal deformability parameter $\tilde{\Lambda}$.

GW190521, detected on 21 May 2019, is arguably the most surprising single event: a merger with progenitor masses 85 and 66 solar masses, producing a 142-solar-mass remnant. The primary mass fell within the pulsational pair-instability mass gap of 65–120 solar masses, suggesting dynamical formation possibly including a previous merger product rather than the isolated-binary evolution channel typical of lighter BBHs. GW190425 (April 2019) was the second BNS detection; GW190412 was a strongly asymmetric BBH with mass ratio near 0.3; and GW200115/GW200105 in early 2020 provided the first confident neutron-star black-hole (NSBH) detections. Binary neutron-star and neutron-star black hole systems provide additional benchmarks for constraining the nuclear equation of state and the physics of compact-object formation (Table 1).

Table 1. Selected milestone gravitational-wave events and their key parameters. [1,2,8]

Event	Date (UT)	Source type	Primary / secondary ($M_\odot$)	Luminosity distance (Mpc)
GW150914	14-Sep-2015	BBH	36 / 29	410
GW151226	26-Dec-2015	BBH	14 / 8	440
GW170817	17-Aug-2017	BNS	1.48 / 1.26	40
GW170814	14-Aug-2017	BBH (3-detector)	30 / 25	540
GW190521	21-May-2019	BBH (upper mass gap)	85 / 66	5300
GW200115	15-Jan-2020	NSBH	5.7 / 1.5	300

5. ASTROPHYSICAL IMPLICATIONS

Gravitational-wave observations have delivered four categories of scientific return. First, they characterise the population of stellar-mass compact objects: mass functions, spin distributions, and formation-channel indicators now constrain isolated-binary evolution versus dynamical-formation scenarios[9]. The black-hole mass distribution extracted from GWTC-3 shows structure including a peak near 35 solar masses plausibly associated with the pulsational pair-instability boundary, a secondary feature near 10 solar masses, and a rising power-law tail at low masses. Spin distributions suggest a significant fraction of sources with low aligned spins, consistent with isolated-binary channels, together with a minority of high-spin or misaligned-spin systems suggestive of dynamical formation in dense stellar environments. Merger-rate densities are approximately 20–40 Gpc^{-3} yr^{-1} for binary black holes, 10–1700 Gpc^{-3} yr^{-1} for binary neutron stars, and 8–140 Gpc^{-3} yr^{-1} for neutron-star–black-hole systems.

Second, gravitational-wave observations test general relativity in the strong-field regime. Constraints include: propagation speed v_g=c to 10^{-15} from GW170817/GRB 170817A coincidence), dispersion, graviton mass $m_g < 10^{-23}$ eV/c^2, parameterised post-Newtonian deviations, black-hole ringdown spectroscopy (quasi-normal modes consistent with Kerr), and tests of the no-hair theorem via multiple-mode ringdown analyses.[10] No statistically significant deviations from general relativity have been observed in any regime probed to date, substantially constraining modified-gravity alternatives.

Third, GW170817 enabled r-process nucleosynthesis measurements through kilonova spectroscopy, confirming compact mergers as principal sources of elements heavier than iron.[2] Infrared spectral features at 0.8 and 2.1 microns in AT2017gfo have been attributed to strontium and possibly other heavy lanthanide-region elements, providing the first direct evidence of r-process nucleosynthesis in a single astrophysical event. Total ejected r-process material of order 0.05 solar masses per event is consistent with binary neutron-star mergers contributing a substantial fraction of galactic heavy elements.

Fourth, standard-siren cosmology measurements exploit the fact that gravitational-wave sources directly encode their luminosity distance, with no reliance on the conventional cosmological distance ladder. Combining a gravitational-wave distance measurement with an electromagnetic redshift (for multi-messenger events like GW170817) or with galaxy-catalogue information (for 'dark sirens') yields independent Hubble-constant measurements.[11] The present uncertainty in the standard-siren H_0 determination is approximately 10–15 per cent, but systematic convergence of many events will provide an independent arbiter of the H_0 tension between local-ladder (SH0ES) and early-universe (Planck CMB) determinations. This programme represents one of the most promising near-term cosmological applications of gravitational-wave astronomy.

6. FUTURE DETECTORS

Planned third-generation ground-based detectors include the Einstein Telescope (Europe) and Cosmic Explorer (USA). The Einstein Telescope is a triangular 10 km underground interferometer with xylophone configuration low-frequency cryogenic interferometer paired with high-frequency high-power interferometer aiming for order-of-magnitude strain sensitivity improvement and extension of the detection band to 3 Hz.[12] Cosmic Explorer proposes 20–40 km L-shaped surface detectors, pushing further into high redshift and enabling detection of stellar-mass binaries throughout cosmic history. These third-generation instruments will detect on the order of 10^5 compact-binary mergers per year, effectively surveying the entire stellar-mass binary population to cosmological distances.

The space-based Laser Interferometer Space Antenna (LISA), scheduled for launch in the mid-2030s, will observe the 10^{-4}–10^{-1} Hz band dominated by massive black-hole mergers, extreme mass-ratio inspirals (EMRIs) of stellar-mass compact objects into supermassive black holes, and a galactic foreground of double white dwarfs.[12] LISA will detect the mergers of 100–10^6 solar-mass black holes throughout cosmic history, probing the seeding and growth of supermassive black holes from the first stars through the present. EMRIs will test general relativity to exquisite precision by mapping the spacetime geometry of supermassive black holes through tens of thousands of orbital cycles.

Pulsar-timing arrays, exploiting the exquisite rotational stability of millisecond pulsars as galactic-scale natural clocks, detect gravitational waves in the nanohertz band (10^{-9}–10^{-6} Hz). In 2023 the NANOGrav, EPTA, PPTA, and IPTA collaborations independently reported evidence of a stochastic gravitational-wave background consistent with the Hellings–Downs correlation signature of an isotropic background[14]. The signal is most plausibly attributed to the unresolved population of supermassive black-hole binary inspirals, though cosmological-origin backgrounds from cosmic strings or phase transitions remain in contention. The nanohertz detection opens the low-frequency gravitational-wave window, complementing the ground-based kilohertz window and the forthcoming millihertz LISA window.

7. DATA ANALYSIS AND INFERENCE CHALLENGES

Detection and parameter estimation of gravitational-wave signals rely on sophisticated Bayesian and frequentist methods that have evolved rapidly with the observational cadence. Template-based matched filtering remains the dominant detection technique for compact-binary coalescences; the search maximises the signal-to-noise ratio against noise-coloured templates, using template banks covering the astrophysically plausible parameter space. Template-bank density is chosen to limit mismatch losses, typically to 3 per cent. Coherent network searches combine data from multiple detectors, improving significance and sky-localisation precision.

Unmodelled burst searches complement template-based methods, targeting signals from supernovae, cosmic strings, and other poorly modelled sources. Coherent WaveBurst, BayesWave, and oLIB pipelines run in parallel with template searches. Long-duration continuous-wave and stochastic-background searches require yet different algorithmic approaches tailored to persistent signals.

Parameter estimation employs Bayesian inference with stochastic sampling. Markov-chain Monte Carlo, nested sampling (dynesty, CPNest), and more recently machine-learning-accelerated samplers (normalising flows, conditional density estimators such as DINGO) have been deployed to reconstruct posteriors over 15–17 source parameters within minutes to hours. Low-latency parameter estimation informs electromagnetic follow-up decisions; offline high-accuracy analyses use the full waveform model library and careful noise characterisation. Systematic uncertainties in waveform models, calibration, and detector noise are propagated through injection studies and coherent framework verification.

8. CONCLUSION

Gravitational-wave astronomy has consolidated into a routine observational science within a decade of first detection. The scientific harvest populations of compact objects, strong-field tests of general relativity, multi-messenger astrophysics, and standard-siren cosmology extends across the traditional disciplinary boundaries of astrophysics, fundamental physics, and cosmology. Future detectors including the Einstein Telescope, Cosmic Explorer, and LISA will deepen this harvest by extending the accessible mass and redshift ranges and by opening the low-frequency space-based window.[12,13] Pulsar-timing arrays have opened the nanohertz window with the first evidence of a stochastic gravitational-wave background in 2023. Together, these complementary windows promise a new era of gravitational-wave observation spanning more than twelve decades in frequency, from 10^{-9} Hz to 10^{4} Hz, and accessing sources from supermassive black-hole binaries through to stellar-mass compact coalescences and the cosmological neutron-star background. The decade ahead will refine the compact-binary census, sharpen cosmological constraints, and probe fundamental-physics regimes inaccessible to any other observational technique.

REFERENCES

1. Abbott BP, Abbott R, Abbott TD, et al.; LIGO Scientific Collaboration; Virgo Collaboration. 2016. Observation of gravitational waves from a binary black hole merger. *Physical Review Letters*. 116(6):061102.
2. Abbott BP, Abbott R, Abbott TD, et al. 2017. Multi-messenger observations of a binary neutron star merger. *Astrophysical Journal Letters*. 848(2):L12.
3. Einstein A. 1916. Näherungsweise Integration der Feldgleichungen der Gravitation. *Sitzungsberichte der Königlich Preussischen Akademie der Wissenschaften (Berlin)*. 688–696.
4. Weisberg JM, Taylor JH. 2005. The relativistic binary pulsar B1913+16: thirty years of observations and analysis. In: *Binary Radio Pulsars*. ASP Conf Ser. 328:25–31.
5. Buonanno A, Sathyaprakash BS. 2015. Sources of gravitational waves: theory and observations. In: *General Relativity and Gravitation: A Centennial Perspective*. Cambridge: Cambridge University Press. p. 287–346.
6. Aasi J, Abbott BP, Abbott R, et al. 2015. Advanced LIGO. *Classical and Quantum Gravity*. 32(7):074001.
7. Tse M, Yu H, Kijbunchoo N, et al. 2019. Quantum-enhanced Advanced LIGO detectors in the era of gravitational-wave astronomy. *Physical Review Letters*. 123(23):231107.
8. Abbott R, Abbott TD, Acernese F, et al. 2023. GWTC-3: compact binary coalescences observed by LIGO and Virgo during the second part of the third observing run. *Physical Review X*. 13(4):041039.
9. Mandel I, Broekgaarden FS. 2022. Rates of compact object coalescences. *Living Reviews in Relativity*. 25(1):1.
10. Abbott BP, Abbott R, Abbott TD, et al. 2016. Tests of general relativity with GW150914. *Physical Review Letters*. 116(22):221101.
11. Abbott BP, Abbott R, Abbott TD, et al. 2017. A gravitational-wave standard siren measurement of the Hubble constant. *Nature*. 551(7678):85–88.
12. Maggiore M, Van Den Broeck C, Bartolo N, et al. 2020. Science case for the Einstein Telescope. *Journal of Cosmology and Astroparticle Physics*. 2020(3):050.
13. Amaro-Seoane P, Audley H, Babak S, et al. 2017. Laser Interferometer Space Antenna. arXiv:1702.00786.
14. Agazie G, Anumarlapudi A, Archibald AM, et al. 2023. The NANOGrav 15 yr data set: evidence for a gravitational-wave background. *Astrophysical Journal Letters*. 951(1):L8.

INTERNATIONAL JOURNAL OF PURE SCIENCE RESEARCH STUDIES (IJPSRS)
(Open Access, Double-Blind Peer Reviewed Journal)
ISSN Online: ISSN Print
EDU SCHOOL
ijpsrs.com

Numerical Methods for Nonlinear Partial Differential Equations: A Comparative Study

Assanu Augustine

Assistant Professor, Department of Mathematics, Marian College Kuttikkanam (Autonomous), Kottayam, India

Article Information

Received: 5th February 2026
Received in revised form: 7th March 2026
Accepted: 8th April 2026
Available online: 14th May 2026

Volume: 2
Issue: 2
DOI: https://doi.org/10.5281/zenodo.20151929

Abstract

Numerical solution of nonlinear partial differential equations is central to contemporary applied mathematics, underpinning models of fluid flow, nonlinear wave propagation, reaction–diffusion, and pattern formation. This paper presents a comparative study of three principal classes of numerical method finite differences, finite elements, and spectral methods applied to the viscous Burgers' equation as a prototype nonlinear problem. Stability, convergence, and computational cost are analysed theoretically and illustrated numerically. The study confirms the complementary strengths of the methods: finite differences offer simplicity and suitability for structured grids; finite elements accommodate complex geometries with provable convergence theory; spectral methods provide exponential convergence for smooth solutions on simple domains. The paper concludes with guidance on method selection for contemporary scientific computing.

Keywords: Numerical PDE, Finite Difference, Finite Element, Spectral Method, Convergence, Burgers' Equation.

1. INTRODUCTION

Nonlinear partial differential equations model a majority of physical phenomena of contemporary scientific interest, from Navier–Stokes fluid dynamics to nonlinear Schrödinger waves, Korteweg–de Vries solitons, Fisher–Kolmogorov–Petrovskii–Piskunov front propagation, Cahn–Hilliard phase field dynamics, and reaction diffusion systems in biology.[1] Despite a rich theoretical apparatus Sobolev spaces, weak solutions, entropy inequalities, viscosity solutions closed-form analytic solutions are rare outside special integrable cases. Numerical methods are therefore the primary investigative tool across engineering, physics, biology, and finance. Method selection is governed by problem geometry (regularity of the domain), regularity of the solution (smooth versus discontinuous), required accuracy (several digits versus machine precision), computational budget, and available software infrastructure.

Three dominant numerical frameworks have emerged over the twentieth century. The finite-difference method, tracing to the work of Courant, Friedrichs, and Lewy in 1928, discretises derivatives by differences on a structured grid. The finite-element method, pioneered in engineering practice by Turner, Clough, Martin, and Topp in the 1950s and formalised mathematically by Ciarlet, Brezzi, and others in the 1970s, uses piecewise-polynomial expansions on unstructured meshes. Spectral methods, developed systematically by Orszag and collaborators in the 1970s, expand the solution in globally defined orthogonal basis functions.[2] Each approach has a distinctive mathematical theory and a characteristic performance profile.

This paper compares the three frameworks with particular attention to convergence rates, stability restrictions, and implementation complexity for nonlinear problems. We use the viscous Burgers' equation as a canonical test problem combining nonlinear convection and diffusion, and illustrate relative performance on

smooth and sharply-gradient regimes. The paper is organised as follows. Section 2 describes the prototype problem and its mathematical properties. Sections 3–5 review the three numerical frameworks. Section 6 presents the comparative analysis, Section 7 discusses time-stepping and parallel aspects, and Section 8 concludes.

2. PROBLEM FORMULATION

The one-dimensional viscous Burgers' equation:

$$u_t + uu_x = vu_{x_x} \tag{1}$$

on the domain [a,b] with appropriate initial and boundary conditions provides a nontrivial benchmark that combines features of hyperbolic conservation laws with parabolic diffusion. For small ν the solution develops sharp gradients characteristic of shocks, challenging the resolution of the numerical scheme. The Cole–Hopf transformation $u = -2v\,\partial_x(\ln \emptyset)$ reduces the Burgers' equation to the linear heat equation for φ, providing an exact reference solution for code verification.[3,4]

The Burgers' equation shares fundamental mathematical structure with the Navier–Stokes equations nonlinear convection balanced by viscous diffusion while remaining tractable enough to enable detailed analysis. The inviscid limit ($\nu \to 0$) exhibits shock formation in finite time from smooth initial data, with entropy conditions singling out the physically correct weak solution. For $\nu > 0$, the solution is smooth for all time but develops internal layers of width $O(\nu)$ near shocks, requiring adequate spatial resolution to capture without spurious oscillations. Figure 1 shows the evolution of a Gaussian initial pulse under the viscous flow.

Beyond Burgers', related nonlinear PDE benchmarks include the KdV equation (soliton propagation), the Kuramoto–Sivashinsky equation (spatiotemporal chaos with dispersion and diffusion), the Allen–Cahn equation (phase field dynamics with sharp interfaces), the nonlinear Schrödinger equation (optical pulse propagation and Bose–Einstein condensates), and the Fisher–KPP equation (travelling-wave fronts in population biology). Each presents distinct numerical challenges preservation of conservation laws, long-time stability, capture of multi-scale structure that illuminate different aspects of numerical method performance.

Fig 1: Evolution of a Gaussian pulse under the viscous Burgers' equation (ν = 0.02), exhibiting steepening followed by viscous regularisation[3].

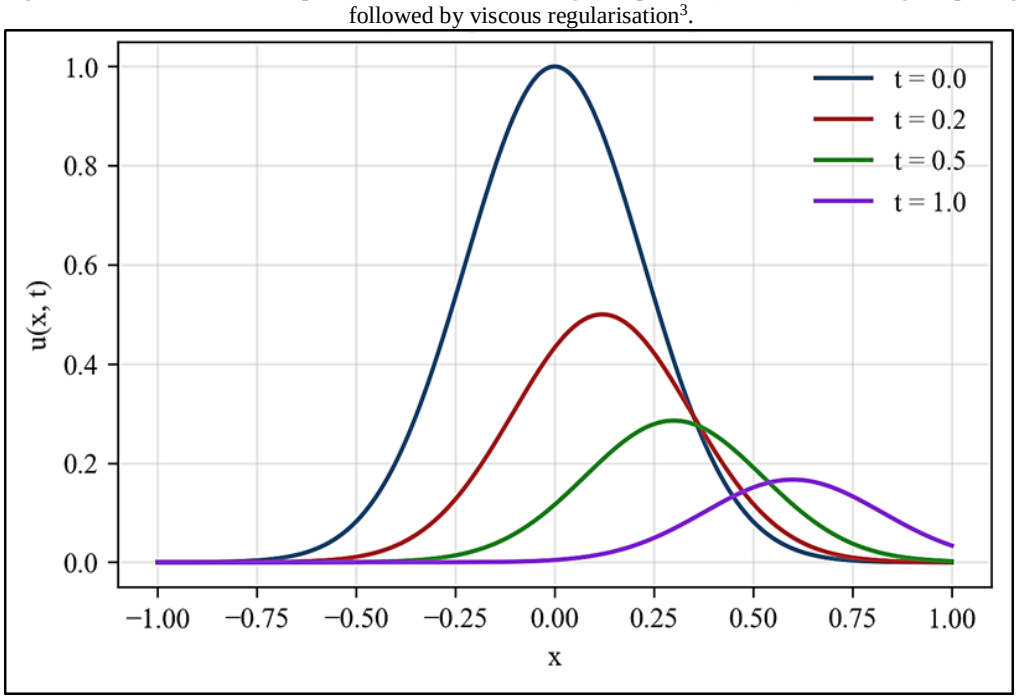

3. FINITE-DIFFERENCE METHODS

Classical finite-difference schemes approximate derivatives by discrete differences on a structured mesh. Taylor expansion about a grid point yields formulas such as the second-order central difference:

$$u'(x_j) \approx \frac{u_{j+1} - u_{j-1}}{2h} \tag{2}$$

the second derivative:

$$u''(x_j) \approx \frac{u_{j+1}-2u_j+u_{j-1}}{h^2} \tag{3}$$

and higher-order counterparts. For convection-dominated problems, upwind differencing biases the stencil toward the direction of characteristic propagation, introducing dissipation that stabilises the scheme at the cost of artificial viscosity.

For Burgers' equation :

$$u_t + uu_x = vu_{xx} \tag{4}$$

the standard explicit upwind scheme combines a second-order central difference for the diffusion with an upwinded approximation of the convective derivative, producing the update:

$$u_j^{n+1} = u_j^n - \Delta t\left[\ u_j^n\ \frac{\left(u_j^n-u_{j-1}^n\right)}{h} - V\frac{(u_{j+1}^n-2u_j^n+u_{j-1}^n)}{h^2}\right] \tag{5}$$

Stability of explicit schemes is governed by the Courant–Friedrichs–Lewy (CFL) condition, which for this formulation requires:

$$\Delta t \le \min\left(\frac{hk}{|u|}, \frac{h^2}{2v}\right) \tag{6}$$

near shocks where $|u_x|$ becomes large, these restrictions can become severe.[5] Implicit schemes (backward Euler, Crank–Nicolson) allow larger stable time steps at the cost of solving algebraic systems at each step.

Higher-order schemes achieve better resolution per grid point. Lax–Wendroff schemes obtain second-order accuracy in both space and time via Taylor-series matching. Essentially non-oscillatory (ENO) and weighted ENO (WENO) schemes adaptively select stencils to avoid crossing discontinuities, attaining formal third- or fifth-order accuracy in smooth regions while controlling oscillations near discontinuities.[6] Compact finite-difference schemes (Padé-type) achieve spectral-like resolution by solving tridiagonal systems for the derivative values, providing sixth-order accuracy with the computational complexity of lower-order schemes. Slope-limited MUSCL (Monotone Upstream-centered Schemes for Conservation Laws) and total-variation-diminishing (TVD) schemes provide robust shock capture for conservation laws while preserving conservation, monotonicity, and discrete maximum principles. These developments have established finite-difference methods as the workhorse of computational fluid dynamics, geophysical modelling, and large-scale direct numerical simulation of turbulence, with codes such as NEK5000, SPECFEM, and PENCIL routinely deploying them n structured grids at exascale.

4. FINITE-ELEMENT METHODS

The finite-element method (FEM) partitions the domain into simplices (triangles in 2D, tetrahedra in 3D) or more general cells, and represents the solution as a piecewise-polynomial expansion:

$$u_h(x,t) = \sum_j u_j(t)\phi_j(x) \tag{7}$$

where the basis functions $\{\phi_j\}$are typically continuous piecewise polynomials of degree k supported on a few adjacent elements (nodal or hierarchical basis). The weak formulation of Burgers' equation, obtained by multiplying by a test function v and integrating by parts, seeks u ∈ V such that :

$$(\partial_t u, v) + (u\ u_x, v) + v(u_x, v_x) = 0 \tag{8}$$

for all v ∈ V, where V is an appropriate Sobolev space. The Galerkin projection onto a finite-dimensional subspace V_h produces a nonlinear system of ordinary differential equations in the nodal coefficients after time-discretisation, typically solved by Newton–Krylov methods with preconditioners tailored to the discretised operator.

The theoretical foundation of FEM is Céa's lemma (for symmetric problems) or the inf-sup (Babuška–Brezzi) condition (for saddle-point problems such as Stokes flow or mixed formulations), combined with the Bramble–Hilbert lemma which provides interpolation estimates of the form:

$$\|u - I_h u\|_{H^s} \le Ch^{k+1-s}\|u\|_{H^{k+1}} \tag{9}$$

for sufficiently smooth u. A priori error bounds for Galerkin approximations then take the form :

$$\|u - u_h\|_{H^1} \leq Ch^k \quad (10)$$

where k is the polynomial degree[7]. For convection-dominated regimes, streamline-upwind Petrov–Galerkin (SUPG) and Galerkin-least-squares (GLS) stabilisations add element-wise residual terms to suppress spurious oscillations without compromising optimal convergence rates.

FEM adapts naturally to complex geometries and local mesh refinement. Adaptive finite-element methods (AFEM) with a posteriori error estimation residual-based, recovery-based, hierarchical, or dual-weighted dynamically refine the mesh where errors are large and coarsen where they are small, yielding quasi-optimal complexity.[8] The hp-finite-element method combines mesh refinement (h-adaptivity) with local polynomial-degree variation (p-adaptivity), achieving exponential convergence on problems with isolated singularities. Discontinuous Galerkin (DG) methods drop inter-element continuity in favour of numerical fluxes matching discontinuity-preserving stencils from finite-volume methods, combining high-order accuracy with shock-capturing robustness; DG has become prominent in electromagnetics, compressible flow, and seismic wave propagation. Modern FEM implementations FEniCS, Firedrake, deal.II, Nektar++ support arbitrary order elements, mixed elements, hp-adaptivity, and parallel solvers, making FEM the dominant framework in structural engineering and multi-physics simulation.

5. SPECTRAL METHODS

Spectral methods expand the solution as:

$$U_N(x,t) = \sum_{k=1}^{N} a_k(t)\phi_k(x) \quad (11)$$

In globally defined basis functions: Fourier series for periodic domains, Chebyshev or Legendre polynomials for bounded intervals on $[-1,1]$. The Gauss–Lobatto collocation nodes associated with these bases provide quadrature rules of very high precision, enabling efficient computation of inner products and nonlinear products. For smooth solutions the truncation error of a spectral expansion decays faster than any algebraic order exponentially in N for analytic solutions a property termed spectral or exponential convergence.[9] This property makes spectral methods the preferred choice for simulations where many digits of accuracy are required, or where scale separation over many decades demands efficient capture of small-scale features with modest resolution.

Spectral methods operate in either the Galerkin or the collocation framework. In the Galerkin approach, expansion coefficients are determined from projection conditions; for nonlinear terms, products in physical space correspond to convolutions in spectral space, which are computed efficiently by transforming to physical space (pseudospectral evaluation). The fast Fourier transform reduces this operation to O(N log N) per evaluation. The 'aliasing error' arising from incomplete quadrature of nonlinear products can be controlled by the 2/3 de-aliasing rule or by adding spectral viscosity. Galerkin methods preserve conservation properties exactly when the bilinear form is symmetric; collocation is algorithmically simpler but may not exactly conserve invariants.

Spectral methods are restricted by the geometric complexity of the basis; for nontrivial geometries, hybrid spectral-element methods (SEM) combine global high-order expansions within each element with C^0 continuity across elements, providing geometric flexibility at the cost of some spectral convergence rate.[10] SEM has been applied widely in ocean modelling, seismic wave propagation, and direct numerical simulation of turbulence in complex geometries, with codes such as Nek5000 and SPECFEM3D scaling to tens of thousands of processors. The discontinuous Galerkin spectral-element method combines DG fluxes with SEM volume integration, providing a flexible high-order framework for nonlinear conservation laws.

6. COMPARATIVE ANALYSIS

Figure 2 shows the L^2 error as a function of mesh size for each method applied to a smooth reference solution of the Burgers' equation. The finite-difference and finite-element schemes exhibit algebraic convergence of order p in h, while the spectral method exhibits exponential convergence until arithmetic precision is reached. This qualitative difference is dramatic in practice: for engineering accuracy (three to five digits), finite-difference and finite-element methods are typically competitive with or superior to spectral methods given their geometric flexibility; but for research-grade simulations demanding six to twelve digits, the spectral method's exponential convergence is decisive.

Method selection depends on several application characteristics. For regular rectangular domains with smooth solutions such as high-accuracy direct numerical simulation of isotropic turbulence in a periodic box spectral methods provide unmatched efficiency. For engineering domains with complex boundaries, non-smooth solutions, or coupled multi-physics (fluid structure interaction, electromagnetics with material interfaces, biomechanics) finite-element methods are preferred for their flexibility and mature software stack. For simulations on structured grids where shock capture is critical compressible fluid dynamics, seismic wave propagation, magnetohydrodynamics high-order finite-difference methods (WENO, compact differencing) balance accuracy with efficiency.

Table 1 summarises the principal characteristics across three axes of comparison: geometric flexibility, convergence rate, and nonlinear-term treatment. Beyond these three classical methods, contemporary practice increasingly uses hybrid approaches spectral elements, discontinuous Galerkin, hp-adaptive finite elements, mesh-free radial basis functions, and boundary-integral methods that combine features of multiple frameworks to address specific problem classes. Error estimation, grid adaptation, and multi-scale coupling have all matured into systematic components of modern PDE computation, supported by open-source libraries and well-documented benchmarks against which new methods can be evaluated.

Fig 2: L² error versus mesh size h for a smooth reference solution. The spectral method's exponential convergence is evident at moderate N.[9,10]

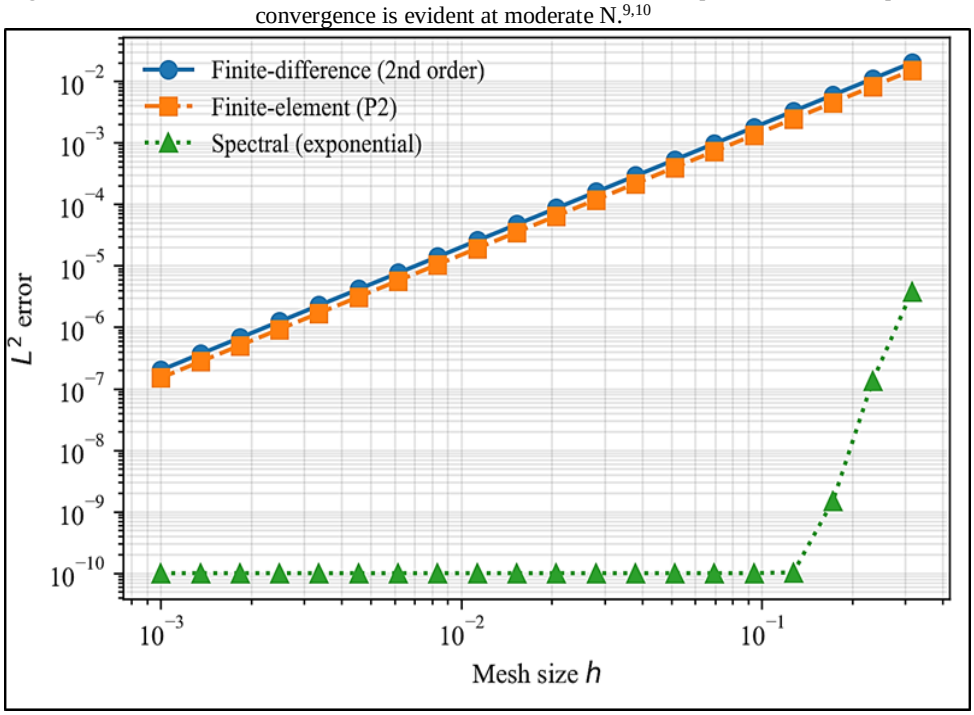

Table 1. Comparative properties of the three numerical frameworks. [5,7,9]

Property	Finite difference	Finite element	Spectral
Geometric flexibility	Structured grids only	Arbitrary domains	Simple domains only
Convergence (smooth u)	Algebraic (order p)	Algebraic (order k)	Exponential
Nonlinear terms	Direct point-wise eval.	Quadrature on elements	Pseudospectral via FFT
Shock capturing	ENO/WENO extensions	Stabilised + AMR	Spectral viscosity
Memory complexity	O(N)	O(N)	O(N log N)
Typical domains	Fluids, seismics	Structural, multi-physics	Turbulence, astrophysics

7. TIME-STEPPING, LINEAR SOLVERS, AND PARALLELISM

Time-discretisation is central to unsteady nonlinear PDE simulation. Explicit Runge–Kutta schemes (classical fourth-order RK4, strong-stability-preserving SSPRK3) offer ease of implementation and good accuracy for advection-dominated regimes, at the cost of CFL-constrained time steps. Implicit schemes (backward Euler, Crank–Nicolson, BDF2–6, DIRK) permit larger steps for stiff diffusive problems, requiring the solution of algebraic systems per step. Implicit–explicit (IMEX) schemes combine explicit treatment of nonlinear convection with implicit treatment of diffusion, capturing the principal stiff behaviour efficiently.

Linear-system solution for implicit schemes dominates the computational cost of large-scale simulations. Sparse direct methods (MUMPS, UMFPACK, PARDISO) work well for moderate 2D problems; iterative Krylov methods (GMRES, BiCGStab, CG for symmetric problems) with algebraic or geometric multigrid preconditioners scale to problems with hundreds of millions of unknowns. For nonlinear problems Newton–Krylov methods with matrix-free Jacobian–vector products avoid explicit Jacobian assembly. The Fast Multipole Method and hierarchical matrix (H-matrix) representations provide near-linear complexity for boundary-integral formulations and kernel-based methods.

Parallel computing has become inseparable from large-scale PDE simulation. Domain decomposition (Schwarz, balanced partitioning), shared-memory multi-threading, and GPU acceleration are widely supported; finite-difference and spectral-element codes routinely run on exascale platforms. The recent emergence of physics-informed neural networks (PINNs) and operator-learning methods (Fourier neural operators, DeepONets) suggests complementary data-driven routes, particularly for high-dimensional parameter spaces and inverse problems, though rigorous convergence and error analysis for these approaches remains an active research area.

8. CONCLUSION

The three classical numerical frameworks remain complementary. Finite differences dominate where structured grids and efficient implementations are priorities particularly geophysical modelling, atmospheric simulation, and structured-grid turbulence direct numerical simulation. Finite elements remain the standard in engineering for geometric complexity and rigorous error analysis, underpinning essentially all structural-mechanics and multi-physics simulation software. Spectral methods are the tool of choice for smooth-solution simulations demanding the highest attainable accuracy, notably in turbulence theory, astrophysics, and climate modelling. Modern large-scale simulations increasingly use hybrid approaches spectral-element, discontinuous Galerkin, mesh-free methods, and physics-informed machine learning that combine the strengths of multiple frameworks.[11] The field continues to advance on three fronts: algorithmic innovation reducing asymptotic complexity, implementation engineering for emerging heterogeneous computing platforms, and integration of classical numerics with data-driven learning approaches. Together these developments will sustain numerical PDE as a central tool of applied mathematics through the coming decade.

REFERENCES

1. Evans LC. 2010. *Partial differential equations*. 2nd ed. Providence (RI): American Mathematical Society.
2. Quarteroni A, Valli A. 1994. *Numerical approximation of partial differential equations*. Berlin: Springer.
3. Burgers JM. 1948. A mathematical model illustrating the theory of turbulence. *Adv Appl Mech*. 1:171–199.
4. Hopf E. 1950. The partial differential equation u_t + u u_x = μ u_xx. *Commun Pure Appl Math*. 3(3):201–230.
5. Courant R, Friedrichs K, Lewy H. 1928. Über die partiellen Differenzengleichungen der mathematischen Physik. *Math Ann*. 100:32–74.
6. Shu CW, Osher S. 1988. Efficient implementation of essentially non-oscillatory shock-capturing schemes. *J Comput Phys*. 77(2):439–471.
7. Brenner SC, Scott LR. 2008. *The mathematical theory of finite element methods*. 3rd ed. New York: Springer.
8. Verfürth R. 2013. *A posteriori error estimation techniques for finite element methods*. Oxford: Oxford University Press.
9. Canuto C, Hussaini MY, Quarteroni A, Zang TA. 2006. *Spectral methods: fundamentals in single domains*. Berlin: Springer.
10. Trefethen LN. 2000. *Spectral methods in MATLAB*. Philadelphia: SIAM.
11. Hesthaven JS, Warburton T. 2008. *Nodal discontinuous Galerkin methods: algorithms, analysis, and applications*. New York: Springer.

INTERNATIONAL JOURNAL OF PURE SCIENCE RESEARCH STUDIES (IJPSRS)
(Open Access, Double-Blind Peer Reviewed Journal)
ISSN Online: ISSN Print
EDU SCHOOL ijpsrs.com

Quantum Entanglement: Foundations and Applications in Quantum Information Science

Vimala George

Associate Professor, Department of Physics, At. Xavier's College for Women (Autonomous), Aluva, India

Article Information

Received: 7th February 2026
Received in revised form: 10th March 2026
Accepted: 13th April 206
Available online: 14th May 2026

Volume: 2
Issue: 2
DOI: https://doi.org/10.5281/zenodo.20152281

Abstract

Quantum entanglement is a non-classical correlation between quantum systems that cannot be accounted for by any local hidden-variable theory. Since its articulation in the Einstein-Podolsky-Rosen paper of 1935 and its formal testability through Bell's theorem in 1964, entanglement has evolved from a philosophical puzzle into the central resource of quantum information science. This review surveys the conceptual foundations of entanglement, the experimental record culminating in loophole-free Bell tests, and applications including quantum key distribution, quantum teleportation, and measurement-based quantum computation. We summarise quantitative results of representative Bell experiments, discuss entanglement measures for mixed states, and outline recent developments in long-distance entanglement distribution via satellites and quantum repeaters. Persistent challenges decoherence, certification of high-dimensional entanglement, and scalable distribution are identified as active frontiers of research.

Keywords: Quantum Entanglement, Bell Inequalities, Quantum Information, Teleportation, QKD, Decoherence

1. INTRODUCTION

The concept of entanglement was introduced in the 1935 paper of Einstein, Podolsky and Rosen, who argued that quantum mechanics must be incomplete because it predicted perfect correlations between spatially separated subsystems in a manner apparently at variance with local realism.[1] Schrödinger named the phenomenon 'Verschränkung' (entanglement) and identified it as 'the characteristic trait of quantum mechanics, the one that enforces its entire departure from classical lines of thought'. EPR proposed a thought-experiment in which two particles emitted from a common source carry perfectly correlated positions and momenta; measuring one particle appeared to predict with certainty the outcome on the other, seemingly violating what they termed the criterion of physical reality. The debate remained philosophical for almost three decades until Bell, in 1964, derived inequalities constraining any local hidden-variable theory and showed that quantum mechanics predicted their violation.[2] Bell's achievement was to transform a metaphysical dispute into a laboratory-testable proposition.

Experimental confirmation began with Clauser, Horne, Shimony and Holt in 1969, who derived a practical variant of Bell's inequality suitable for imperfect detectors, and with the landmark optical experiments of Aspect and colleagues in 1981–1982 using Ca-cascade photon sources.[3] The Aspect experiments, and subsequent refinements closing successive loopholes, progressively eliminated classical explanations for the observed correlations, culminating in the 2015 loophole-free tests conducted independently at Delft, Vienna, and NIST Boulder. In 2022, Alain Aspect, John Clauser, and Anton Zeilinger were awarded the Nobel Prize in Physics for experiments with entangled photons, establishing the violation of Bell inequalities, and pioneering quantum information science.

Over the last three decades, entanglement has moved from foundational study to practical resource. Quantum key distribution, quantum teleportation, superdense coding, and measurement-based quantum computation all exploit entanglement as a non-classical resource irreducible to classical communication channels.[4,5] The field has correspondingly developed a rich mathematical apparatus of entanglement measures, together with experimental protocols for witnessing and quantifying entanglement in laboratory systems ranging from photon pairs through trapped ions, neutral atoms in optical tweezers, nitrogen-vacancy centres in diamond, to superconducting transmon qubits. The 2020s have seen entanglement-based technologies move beyond laboratory demonstration: satellite-based quantum key distribution is operational in China; the first multi-node quantum networks are functioning in the Netherlands, the United States, and China; and 1000-qubit entanglement-capable processors have been demonstrated on several platforms.

This review is organised as follows. Section 2 presents the theoretical foundations of entanglement, including Bell inequalities and the mathematical structure of entangled states. Section 3 summarises the experimental record leading to loophole-free Bell tests. Section 4 surveys principal applications in quantum information. Section 5 reviews entanglement measures and certification techniques for mixed states. Section 6 identifies current challenges and Section 7 concludes.

2. THEORETICAL FOUNDATIONS

A pure bipartite state $|\psi\rangle_{AB} \in H_A \otimes H_B$ is entangled if it cannot be written as a tensor product $|\phi\rangle_A \otimes |\chi\rangle_B$. The four maximally entangled Bell states:

$$|\Phi^{\pm}\rangle = \frac{1}{\sqrt{2}}(|00\rangle \pm |11\rangle), \quad |\Psi^{\pm}\rangle = \frac{1}{\sqrt{2}}(|01\rangle \pm |10\rangle) \tag{1}$$

serve as a canonical basis for two qubits and exhibit the maximum non-classical correlation possible for a bipartite two-level system. A useful diagnostic is the Schmidt decomposition: any pure bipartite state admits the form:

$$|\psi\rangle = \sum_i \sqrt{\lambda_i}\,|i\rangle_A \otimes |i\rangle_B \text{ with } \lambda_i \geq 0, \quad \sum_i \lambda_i = 1 \tag{2}$$

The state is entangled if and only if more than one Schmidt coefficient is nonzero; the Schmidt rank and the entropy $S(\rho_A) = -\mathrm{Tr}(\rho_A \log \rho_A)$ of the reduced density matrix $\rho_A = \mathrm{Tr}_B\,(|\psi\rangle\langle\psi|)$ provide canonical entanglement measures for pure states. For mixed states, the separability problem is more subtle. A state ρ_{AB} is separable if it admits the form:

$$\rho_{AB} = \sum_k \rho_k\, \rho_k^A \otimes \rho_k^B \tag{3}$$

$$\rho_k \geq 0 \text{ and } \sum_k \rho_k = 1 \tag{4}$$

otherwise it is entangled.[6] The Peres–Horodecki partial-transpose criterion provides a necessary condition for separability: the partial transpose ρ^{TB} of a separable state has only non-negative eigenvalues. For 2×2 and 2×3 systems the criterion is also sufficient (Horodecki theorem), but for higher-dimensional systems bound entangled states exist whose partial transpose is positive despite non-separability. These bound-entangled states cannot be distilled to singlets but still display non-classical properties and can activate distillable entanglement in conjunction with other states.

Bell inequalities provide operational tests. The Clauser–Horne–Shimony–Holt (CHSH) form bounds the linear combination $S = E(a,b) + E(a,b') + E(a',b) - E(a',b')$ by $|S| \leq 2$ under local realism, whereas quantum mechanics permits $|S| \leq 2\sqrt{2}$ (Tsirelson's bound), attained when the measurement settings are chosen on maximally entangled singlet states. The correlation $E(a,b) = -\cos(\theta_{ab})$ predicted for the singlet state differs fundamentally from the linear bound obtainable under local realism (Figure 1).[2,3] Several generalisations extend Bell inequalities to more observers (Mermin–GHZ), more measurement settings (I3322, chained inequalities), and higher-dimensional systems. The GHZ argument, introduced by Greenberger, Horne, and Zeilinger, provides a deterministic refutation of local realism using three-particle entanglement without statistical reasoning: the quantum predictions for certain measurement combinations are strictly incompatible with any local hidden-variable assignment, not merely statistically suppressed.

The information-theoretic perspective, consolidated in the 1990s, treats entanglement as a resource that can be manipulated under the constraint of local operations and classical communication (LOCC). Under LOCC, entanglement cannot be generated from separable states and can only decrease on average, defining a meaningful partial order on entangled states. This framework permits the definition of rate-based measures such as distillable entanglement E_D (the asymptotic rate of Bell-pair extraction) and entanglement cost E_C(the asymptotic rate of Bell-pair consumption needed for preparation); for pure states $E_D = E_C = S(\rho A)$, but for mixed states the two quantities are generally different, and their gap quantifies irreversibility in entanglement manipulation.

Fig 1: Quantum prediction E(a,b) = −cos θ for singlet correlations compared with the maximum slope permitted by local hidden-variable theories. The deviation is the origin of Bell inequality violations.[2,3]

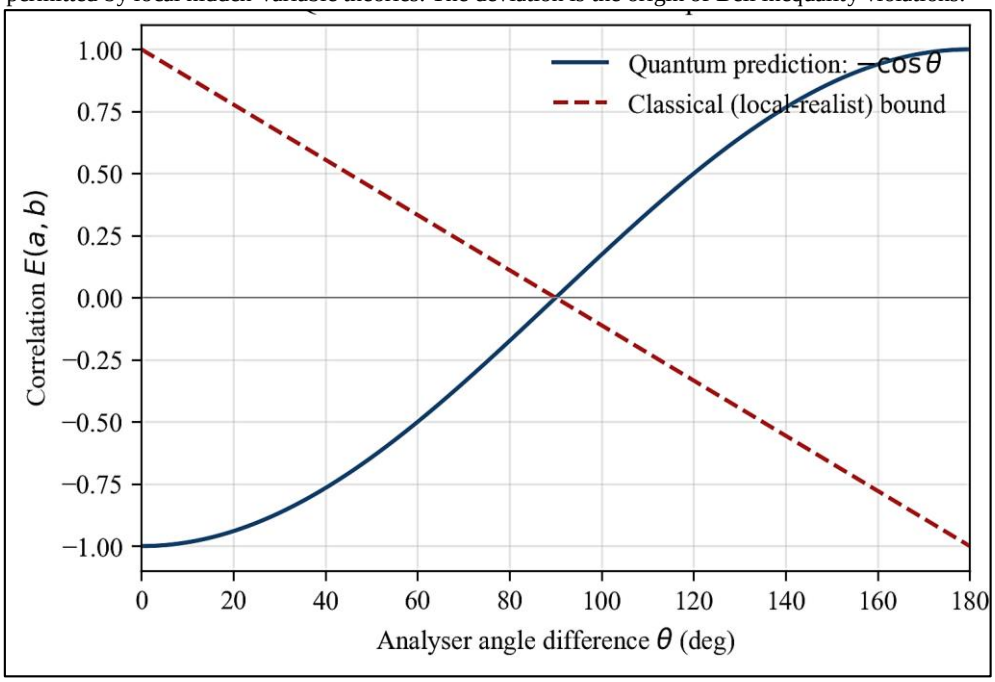

3. EXPERIMENTAL VERIFICATION

Bell-inequality experiments have been refined progressively over six decades. The first experimental test was performed by Freedman and Clauser in 1972 using photons from a Ca cascade; the observed correlations violated the CHSH inequality at approximately six standard deviations. These early experiments were limited by low detection efficiency and by the static nature of the analyser settings, which together allowed local-realist evasions via the 'fair-sampling' and 'communication' loopholes.

The Aspect experiments of the early 1980s[3] closed a major loophole by switching analyser settings while photons were in flight, with switching interval shorter than the light transit time between analysers ensuring that no subluminal signal could coordinate the measurement outcomes. The 1998 Weihs experiment refined this using truly random switching driven by independent physical random-number generators, achieving convincing violations under strict locality conditions. Nevertheless, critics continued to identify residual loopholes: the 'detection loophole' (the detected fraction might be a biased sub-ensemble of emissions), the 'locality loophole' (residual subluminal communication via experimental apparatus), and the 'freedom-of-choice loophole' (measurement settings might themselves be causally correlated with hidden variables).

Loophole-free tests were reported almost simultaneously in 2015. The Delft group, led by Hensen and Hanson, used electronic spins in nitrogen-vacancy (NV) centres separated by 1.3 km, with entanglement swapping via photonic Bell-state measurement and post-selection by heralding.[7] Because NV spins can be read out with essentially unit efficiency, the detection loophole was closed; the physical separation exceeded the operational timescale ensuring spacelike separation. The measured CHSH parameter was 2.42 ± 0.20, corresponding to a p-value of 0.039 under local realism. Vienna (Giustina et al.) and NIST-Boulder (Shalm et al.) simultaneously reported photon-based loophole-free tests using superconducting-nanowire single-photon detectors with ~75% efficiency and spacelike-separated random number-generators for setting choice.[8,9] The measured p-values were below 10^{-6} and 10^{-9} respectively, establishing violations at overwhelming statistical significance.

Subsequent experiments have extended loophole-free testing to cosmological sources of randomness (using photons from distant quasars to set measurement bases, thereby addressing the freedom-of-choice loophole on cosmological timescales) and to hybrid systems combining NV centres with photonic entanglement distribution. Bell-type tests have been performed in hybrid settings involving trapped ions, neutral atoms, superconducting qubits, and solid-state spins, consistently confirming the quantum predictions. Figure 2 shows the canonical coincidence-based experimental geometry for Bell tests.

Fig 2. Schematic of a Bell-state coincidence experiment

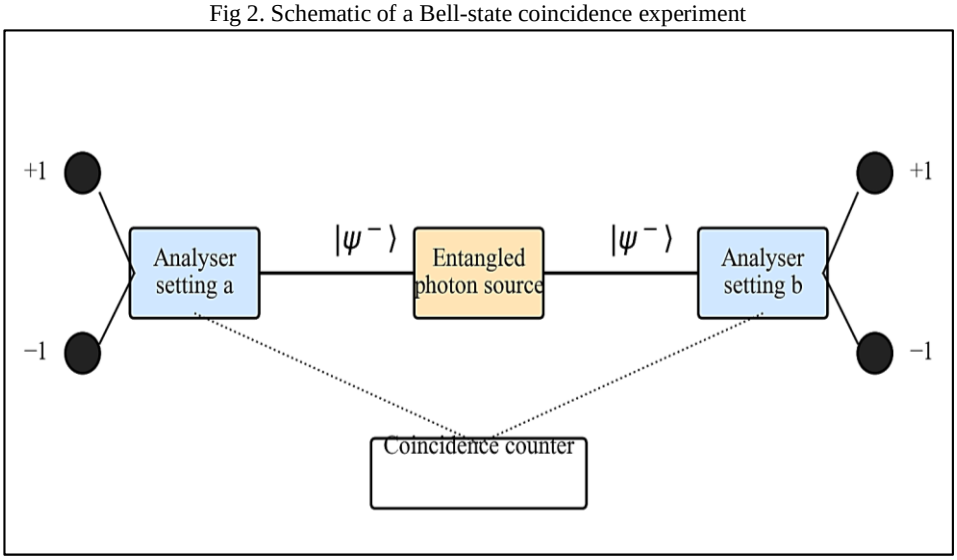

A source emits entangled photon pairs; two distant analysers with independently chosen settings measure each photon, and coincidence counts reveal the quantum correlations.[3, 7]

Table 1. Summary of representative Bell-test experiments and measured CHSH parameter S (quantum bound $2\sqrt{2} \approx 2.828$). [3,7,8,9]

Experiment	Year	System	Measured S	Statistical significance
Aspect et al.	1982	Entangled photons (Ca cascade)	2.697 ± 0.015	~5σ
Weihs et al.	1998	Photons, strict locality	2.73 ± 0.02	>30σ
Hensen et al.	2015	NV centres, 1.3 km	2.42 ± 0.20	p = 0.039
Giustina et al.	2015	Photons, loophole-free	2.10 ± 0.12	$p < 10^{-9}$
Shalm et al.	2015	Photons, loophole-free	2.00 ± 0.06	$p < 10^{-6}$

4. APPLICATIONS IN QUANTUM INFORMATION

Entanglement is the principal non-classical resource underpinning quantum information processing. Several distinct protocols exploit entanglement in functionally different ways, each of which has matured from theoretical proposal to laboratory demonstration.

Quantum key distribution (QKD), in its entanglement-based form formulated by Ekert in 1991, uses the violation of Bell inequalities as a certification of security against eavesdroppers regardless of the underlying hardware the basis of device-independent cryptography.[4] The protocol proceeds as follows: a source distributes entangled pairs to Alice and Bob, who measure their shares in randomly chosen bases; a subset of outcomes is publicly disclosed to verify a Bell-inequality violation, establishing that the correlations cannot be explained by pre-shared classical information, and the remaining outcomes constitute the secret key. The decoy-state BB84 variant (based on single-particle superposition rather than entanglement) achieves higher key rates at shorter distances and is now commercially deployed in metropolitan networks in Europe, China, and the United States. Device-independent QKD, based on Bell-inequality violations, provides stronger security guarantees but requires substantially higher detection efficiency and has only recently been demonstrated with practical key rates.

Quantum teleportation, proposed by Bennett and colleagues in 1993 and first demonstrated with photons in 1997, transfers an unknown quantum state using one shared entangled pair and two bits of classical communication.[10] Importantly, the protocol does not involve physical transport of the particle carrying the state, and classical communication bandwidth is required for completion preserving relativistic causality. Teleportation has been demonstrated across free-space links of hundreds of kilometres, between matter and light, between different physical systems, and across a satellite-to-ground channel using the Micius satellite. It underpins quantum repeaters, entanglement swapping, and modular quantum computing architectures that distribute computation across multiple processors.

Measurement-based (or one-way) quantum computation on cluster states reduces the circuit model to sequential adaptive measurements on a pre-prepared highly entangled resource state.[11] The universal computational power of one-way quantum computation has been demonstrated on photonic and atomic platforms; its architectural advantage is that physical operations are restricted to local measurements and classical

feedforward, potentially reducing hardware requirements for fault-tolerant implementation. Superdense coding, introduced by Bennett and Wiesner in 1992, uses a shared entangled pair to transmit two bits of classical information via a single qubit, doubling the classical channel capacity. Quantum error-correcting codes, such as the surface code now implemented on superconducting processors, rely on entangled logical-qubit encodings to protect quantum information from decoherence through redundant distributed encoding across many physical qubits.

Satellite-based entanglement distribution has become practical. The Chinese Micius satellite, launched in 2016, demonstrated distribution of entangled photon pairs between ground stations separated by over 1 200 km, with Bell-inequality violations observed in 2017.[12] Subsequent missions have extended entanglement distribution to intercontinental distances (Beijing–Vienna, 7 600 km) and established the first satellite-to-satellite entanglement links. The European Union's EuroQCI initiative and the US Quantum Internet Blueprint aim to deploy fibre-based and satellite-based quantum networks over the next decade. Combined with ground-based fibre networks, such platforms are enabling the first generation of quantum internet prototypes capable of supporting distributed quantum computation, blind quantum computing (in which a client delegates computation to a server without revealing the computation itself), and clock-synchronisation beyond the standard quantum limit.

5. ENTANGLEMENT MEASURES AND CERTIFICATION

For mixed states the separability problem is computationally hard in general formally, deciding separability is NP-hard as the dimension grows. This has motivated the development of a rich taxonomy of entanglement measures adapted to different scenarios and computational constraints. Standard measures include entanglement of formation E_F, distillable entanglement:

$$E_{D,\text{negativity}}N(\rho) = \frac{\|\rho^{T_B}\|_1 - 1}{2} \tag{5}$$

logarithmic negativity, relative entropy of entanglement, and the concurrence C(ρ) introduced by Wootters for two-qubit systems.[6,13] Concurrence admits a closed-form expression in terms of the eigenvalues of $\rho(\sigma_y \otimes \sigma_y)\rho^*(\sigma_y \oplus \sigma_y)$, and remains one of the few exactly computable measures on mixed-state ensembles. For larger systems, lower bounds on entanglement can be obtained from convex-roof constructions, and concurrence-like quantities generalise via the so-called G-concurrence for higher-dimensional systems.

Entanglement witnesses Hermitian operators W whose expectation ⟨W⟩ is non-negative on all separable states but can be negative on some entangled states provide experimentally accessible certification, and are widely used in multi-qubit laboratory characterisation. Witnesses constructed from stabiliser measurements are particularly powerful for graph states and cluster states, enabling scalable entanglement detection in photonic, atomic, and solid-state systems. Steering inequalities, introduced by Wiseman and colleagues, provide a third level of correlation hierarchy between local realism and quantum mechanics and have been demonstrated experimentally; steering is strictly weaker than Bell non-locality but stronger than entanglement.

Device-independent certification, drawing on Bell-inequality violation, allows certification of entanglement and randomness without trusting the measurement devices. This framework underpins device-independent QKD, randomness amplification from weak seeds, and self-testing protocols in which a specific quantum state and measurements can be uniquely identified from observed statistics alone. Full quantum-state tomography remains the gold standard for complete state characterisation but scales exponentially in system size; shadow tomography, compressed sensing, and neural-network-based tomography are recent alternatives reducing sample complexity.

6. CURRENT CHALLENGES

Three challenges dominate the present research agenda. First, decoherence continues to limit the lifetime of entangled states in realistic environments. Environmental coupling produces amplitude damping and phase randomisation, which degrade entanglement faster than classical correlations a phenomenon termed entanglement sudden death in some regimes. Dynamical decoupling using sequences of control pulses (Carr–Purcell–Meiboom–Gill, Uhrig) extends coherence times by decoupling the system from low-frequency environmental noise. Topological encoding (Majorana qubits, surface codes) and concatenated error-correcting codes distribute logical information across many physical qubits, protecting against local errors while introducing the overhead of additional hardware and operation complexity.[14] The threshold theorem establishes that with sufficiently low error rate per gate, arbitrarily long computations become feasible.

Second, certification of entanglement in high-dimensional and many-body systems requires scalable protocols that go beyond full tomography. Entanglement in large systems displays qualitatively new phenomena: area laws for entropy in gapped ground states, volume laws in thermalising systems, topological entanglement entropy characterising topologically-ordered phases, and measurement-induced phase transitions in monitored

quantum circuits. Tensor-network representations (matrix product states, PEPS, MERA) provide efficient encodings for low-entanglement states and are at the heart of numerical many-body quantum physics.

Third, entanglement distribution over global distances requires quantum repeaters combining entanglement swapping, purification, and quantum memories with sufficient coherence times; several competing platforms rare-earth-ion crystals, atomic ensembles (DLCZ protocol), NV centres in diamond, and trapped-ion ensembles are being pursued.[15] A repeater architecture divides the total channel into segments, generates entanglement across each segment, stores entanglement in local memories, and hierarchically combines segments via entanglement swapping and distillation to produce high-fidelity long-distance entanglement. Recent demonstrations have achieved two- and three-node repeater operation with entanglement fidelities exceeding classical benchmarks, although end-to-end quantum network throughput remains orders of magnitude below what is required for practical quantum-internet applications.

7. MANY-BODY ENTANGLEMENT AND RECENT FRONTIERS

While early quantum-information research focused on two- and few-particle entanglement, recent years have witnessed rapid development of many-body entanglement as a diagnostic tool for phases of matter and a resource for quantum simulation. The entanglement entropy of a subsystem obeys an area law in gapped ground states of local Hamiltonians, a fundamental result that justifies the efficiency of tensor-network representations. In critical one-dimensional systems, the entanglement entropy diverges logarithmically with subsystem size, with a universal coefficient given by the central charge of the underlying conformal field theory linking entanglement directly to universality classes of quantum phase transitions.

Topologically ordered phases of matter, such as fractional quantum Hall states and spin liquids, are characterised by topological entanglement entropy: a constant correction to the area law that depends on the total quantum dimension of the underlying topological order. The non-local encoding of quantum information in such phases protects against local decoherence and provides a natural route to fault-tolerant quantum computing through topological qubits (Kitaev surface code, Majorana zero modes). Recent experiments on superconducting processors have realised small-scale surface-code logical qubits, demonstrating the 'below-threshold' regime required for scalable fault tolerance.

Measurement-induced entanglement phase transitions, discovered in 2019, occur in quantum circuits with unitary evolution interleaved with random projective measurements: above a critical measurement rate, the steady-state volume-law entanglement collapses to area-law entanglement. This phenomenon, with no classical analogue, has become a testbed for understanding the interaction between entanglement generation and decoherence. Quantum simulators including trapped-ion and neutral-atom arrays have begun to observe these transitions experimentally.

8. CONCLUSION

Entanglement has matured from a philosophical curiosity into a laboratory workhorse and a technological resource. Loophole-free Bell tests have closed longstanding debates about local realism; quantum cryptography and teleportation have become operational capabilities; entanglement-based quantum networks are now an engineering agenda; and many-body entanglement has become a unifying language for condensed-matter physics. The awarding of the 2022 Nobel Prize to Aspect, Clauser, and Zeilinger recognises the field's transition from foundations to technology. The next decade is likely to see entanglement distributed routinely across intercontinental distances, fault-tolerant quantum processors of steadily increasing scale, and the practical exploitation of entanglement-enhanced sensing and metrology.[5,12,15] Open frontiers include scalable entanglement certification, thermodynamics of entanglement, the role of entanglement in gauge-gravity duality and quantum gravity, and the integration of entanglement-based protocols with classical communication infrastructure. Entanglement, once considered a source of paradox, has become both a rigorous physical phenomenon and a practical engineering resource.

REFERENCES

1. Einstein A, Podolsky B, Rosen N. Can quantum-mechanical description of physical reality be considered complete? *Physical Review*. 1935;47(10):777–780.
2. Bell JS. On the Einstein Podolsky Rosen paradox. *Physics*. 1964;1(3):195–200.
3. Aspect A, Grangier P, Roger G. Experimental realization of Einstein-Podolsky-Rosen-Bohm gedankenexperiment: a new violation of Bell's inequalities. *Physical Review Letters*. 1982;49(2):91–94.
4. Ekert AK. Quantum cryptography based on Bell's theorem. *Physical Review Letters*. 1991;67(6):661–663.
5. Nielsen MA, Chuang IL. *Quantum computation and quantum information*. 10th anniversary ed. Cambridge: Cambridge University Press; 2010.
6. Horodecki R, Horodecki P, Horodecki M, Horodecki K. Quantum entanglement. *Reviews of Modern Physics*. 2009;81(2):865–942.
7. Hensen B, Bernien H, Dréau AE, et al. Loophole-free Bell inequality violation using electron spins separated by 1.3 kilometres. *Nature*. 2015;526(7575):682–686.

8. Giustina M, Versteegh MAM, Wengerowsky S, et al. Significant-loophole-free test of Bell's theorem with entangled photons. *Physical Review Letters*. 2015;115(25):250401.
9. Shalm LK, Meyer-Scott E, Christensen BG, et al. Strong loophole-free test of local realism. *Physical Review Letters*. 2015;115(25):250402.
10. Bennett CH, Brassard G, Crépeau C, Jozsa R, Peres A, Wootters WK. Teleporting an unknown quantum state via dual classical and Einstein-Podolsky-Rosen channels. *Physical Review Letters*. 1993;70(13):1895–1899.
11. Raussendorf R, Briegel HJ. A one-way quantum computer. *Physical Review Letters*. 2001;86(22):5188–5191.
12. Yin J, Cao Y, Li YH, et al. Satellite-based entanglement distribution over 1200 kilometers. *Science*. 2017;356(6343):1140–1144.
13. Wootters WK. Entanglement of formation of an arbitrary state of two qubits. *Physical Review Letters*. 1998;80(10):2245–2248.
14. Terhal BM. Quantum error correction for quantum memories. *Reviews of Modern Physics*. 2015;87(2):307–346.
15. Briegel HJ, Dür W, Cirac JI, Zoller P. Quantum repeaters: the role of imperfect local operations in quantum communication. *Physical Review Letters*. 1998;81(26):5932–5935.